P1 center network in high-pressure high-temperature diamonds is a readily accessible source of nuclear hyperpolarization at 14 T

Quentin Stern,[1] Jinlei Cui,[1] Raj Chaklashiya,[1,2] Celeste Tobar,[1,3] Martyna Judd,[1,4] Orit Nir-Arad,[5] Daphna Shimon,[6] Ilia Kaminker,[5] Hiroki Takahashi,[7] Jagadishwar R. Sirigiri,[8] & Songi Han[1,2†]

[1] Department of Chemistry, Northwestern University, 633 Clark Street, Evanston, 60208, IL, USA.
[2] Materials Department, University of California, Santa Barbara, 93106, CA, USA
[3] Department of Chemistry and Biochemistry, University of California, Santa Barbara, 93106, CA, USA.
[4] Research School of Chemistry, The Australian National University Canberra, ACT 2605, Australia.
[5] School of Chemistry, Tel-Aviv University, 6997801 Tel-Aviv, Israel.
[6] Institute of Chemistry, Hebrew University of Jerusalem, Jerusalem 9190401, Israel.
[7] JEOL Ltd., Akishima, Tokyo, 196-8558, Japan.
[8] Bridge12 Technologies, Inc., Natick, MA, USA.

[†] Correspondence: songi.han@northwestern.edu

Abstract: We investigate nitrogen substitution defects, also known as P1 centers, in type 1b diamonds as a source of electron spin polarization that is readily transferred to ^{13}C nuclear spins within the diamond matrix at 14 Tesla by dynamic nuclear polarization (DNP) at room temperature down to 35 K. The goal was to obtain a quantitative model for clustered P1 centers in diamonds generated under high pressure and high temperature (HPHT). The study relied on frequency-stepped measurements of DNP profiles under magic angle spinning (MAS) using the mm-wave output of a frequency-tunable gyrotron and a regular superconducting NMR magnet set at a single field. The gyrotron output frequency was controlled via the temperature of the gyrotron cavity over 260 MHz centered around 395.3 GHz and had an output power of ~1 W across this range. We observe ^{13}C on/off signal enhancements of up to 700-fold at room temperature under MAS and in static mode, and 130-fold between 35K and 100 K. Modeling of the experimental results revealed the dominant role of P1 clusters harboring inter-P1 dipolar and exchange couplings exceeding 100 MHz in achieving effective ^{13}C DNP at 14.1 T. Clustered P1 centers may be of great utility in generating highly enhanced ^{13}C NMR signal in high-pressure high-temperature diamond as a source of contrast for NMR and MRI applications, or a major decoherence source in quantum sensing applications.

Introduction

The inherently low sensitivity of nuclear magnetic resonance (NMR) can be increased by several orders of magnitude by polarizing nuclear spins above thermal equilibrium using dynamic nuclear polarization (DNP).[1] This boost in sensitivity allows for the detection of dilute or low population species that would otherwise be well below the limits of standard solid state (SS)-NMR,[2,3] and magnetic resonance imaging (MRI).[4] DNP can also be used indirectly to increase the sensitivity of quantum sensing via ^{13}C NMR magnetometry.[5] In addition, enhancing the bulk nuclear spin hyperpolarization in an inert material is of great interest, owing to the potential for achieving long spin relaxation lifetimes and decoherence times, for quantum information storage,[6] quantum sensing,[7–10] or as a source of strong NMR signals or high MRI

contrast.[11] DNP is a highly promising approach to achieve bulk nuclear spin polarization using intrinsic paramagnetic defects in materials, but the selection or design criteria of defects for achieving high DNP efficiency is rarely discussed.

The DNP method consists of transferring the high polarization of unpaired electron spins of a polarizing agent (PA) to the surrounding nuclear spins by means of millimeter-wave (mm-wave) irradiation at a precise frequency that is determined by the PA, the magnetic field, and the nature of the nuclear spins to be hyperpolarized.[12] Tremendous efforts have been put into the development of PAs for MAS-DNP with high fidelity and desirable properties, but the majority of currently used PAs belong to a surprisingly narrow selection of biradical archetypes consisting of a pair of nitroxides[13] or of a nitroxide and a narrow-line radical such as trityl.[14] On the one hand, these existing biradical PAs enabled transformative NMR and MRI studies.[15–17] On the other hand, these molecular PAs can be less effective for generating high bulk nuclear spin polarization at high magnetic fields exceeding 14 T[18] and at room temperature (RT),[19] and may not offer inert materials property to withstand desirable conditions that may be highly reducing or oxidizing.

We turn our attention to paramagnetic centers in diamonds, given their prominence in being utilized as sensors and probes[20,21] through synthesis, surface modification, functionalization, and other material preparation techniques.[22,23] These paramagnetic centers have been used for quantum sensing or DNP under many experimental conditions, typically at magnetic fields ranging from tens of mT to 7 T.[24–33] Negatively charged nitrogen-vacancy defects (NV^-) can be optically pumped at RT and the electron spin polarization subsequently transferred to the surrounding ^{13}C spins by DNP at low magnetic fields.[25] The resulting hyperpolarized ^{13}C spins have been utilized as qubits for quantum sensing[21] and quantum information processing.[34] Hyperpolarization of ^{13}C spins in nanodiamonds has also been performed at liquid helium temperatures,[24] employing these nanodiamonds as tracers for magnetic resonance imaging (MRI).[11] Bretschneider *et al*. reported ^{13}C DNP enhancements of up to ~300-fold and ~150-fold at 100 K and RT, respectively, using nitrogen defects at a magnetic field of 9.4 T under MAS (referred to as P1 centers, see Figure 1a) in micrometer-size diamonds, with DNP transfer achieved using a 10 W gyrotron.[24,26] Palani *et al*. recently showed that the MAS-DNP enhancement at RT and 9.4 T was improved by moderate spinning and reached saturation using only a few watts of microwave power.[35] Kato *et al.* have reported the use of surface electron spins of nanodiamonds as PAs for MAS-DNP at ultra-low temperature (ULT) down to 30 K, and demonstrated their potential for boosting multidimensional NMR for biomolecular studies. Paramagnetic centers in diamond represent a versatile and promising substrate for DNP[36] with the potential of reaching high signal enhancements at RT while requiring weaker microwave power than conventional MAS-DNP.

Microdiamonds have been used in a number of studies of static DNP at moderate magnetic field (3–7 T).[28–33] Nevzorov *et al*. obtained enhancements up to 1000-fold under static DNP in a high-pressure high-temperature (HPHT) diamond single crystal using a 50 W klystron as the microwave source and using a high-Q EPR resonator at 7 T and RT.[32] The high resulting B_{1e} field of 30 MHz was able to efficiently drive solid effect (SE) transitions. The SE is distinct in its properties and performance from the cross effect (CE) DNP that typically drives ^{13}C hyperpolarization in HPHT diamonds at high magnetic fields.[24,26] Shimon *et al*. showed that ^{13}C-DNP from P1 centers could reach high enhancements at moderate magnetic fields (3.4 and 7 T) and RT in static conditions using solid-state microwave sources outputting hundreds of mW.[28,29] Von Witte *et al*. recently studied the temperature dependence of static DNP at the same fields (3.4 and 7 T) and with similar microwave powers, from 1.7 K to RT and obtained high enhancement across the whole

temperature range.[31] Paramagnetic defects in diamond are known to be distributed non-uniformly, as evidenced for example by Panich *et al.*'s NMR relaxation measurements[37,38] and Shames *et al.*'s half-field EPR measurements.[39] Bussandri *et al*. demonstrated that a large fraction of P1 centers were present as clusters using DNP at 7 T and RT and pulsed EPR at 8 T.[30] Similar conclusions were reached by Nir-Arad *et al.* using DNP, pulsed EPR, and electron-electron double resonance at 7 and 14 T, on a diamond single crystal.[31] However, there are limited studies investigating the spatial distribution and couplings of P1 centers in diamond that critically affect their utility as PAs for DNP at a high magnetic field of 14 T.[31,40]

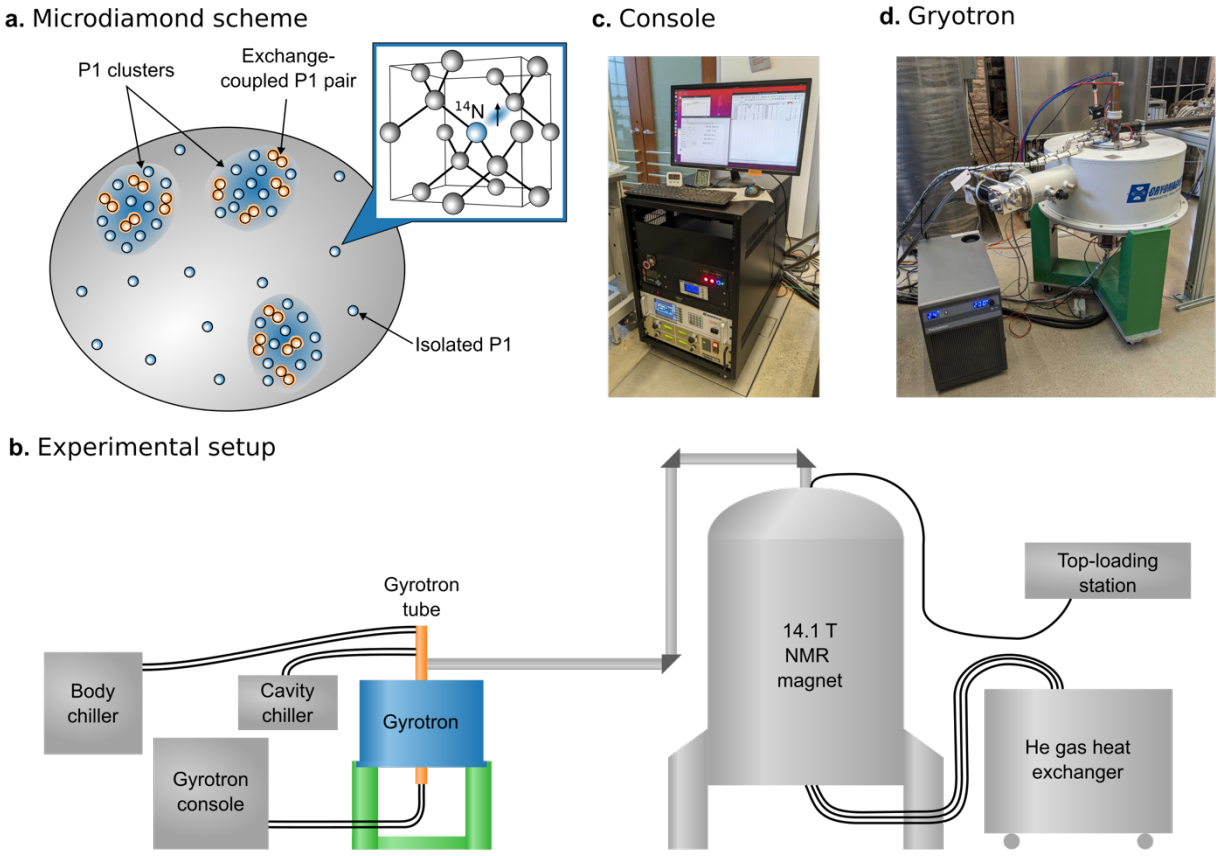

Figure 1: **a**. Scheme of a microdiamond including P1 clusters and isolated P1 centers. The inset shows the crystal structure of a P1 center with the location of the paramagnetic spin-½ electron. **b**. Diagram of the experimental setup. **c,d**. Picture of the console of the gyrotron and the gyrotron itself, respectively.

In the present work, we investigate the ^{13}C-DNP performance of P1 centers in HPHT microdiamonds at 14.1 T across a wide range of experimental conditions, from RT to ULT, under MAS and in static mode. We used a low power gyrotron with tunable frequency, which lifts the necessity for a variable-field magnet to measure the DNP profile, i.e., DNP enhancement as a function of mm-wave frequency (referring to the electromagnetic waves generated by the gyrotron with mm wavelengths, not microwaves, at frequencies exceeding 300 GHz). Frequency-tunable gyrotrons have already been used for MAS-DNP by several groups; Fujiwara, Matsuki and coworkers tuned the frequency of their gyrotron via its magnetic field for MAS-DNP at 14.1 T,[41,42] and Barnes and coworkers via the anode voltage for MAS-DNP at 7 T.[43,44] Both these approaches allow for a large tuning range but result in a highly variable power across the tuning range. Here, we tune the frequency via the temperature of the cavity, which results in a more even power across

the different frequencies, hence allowing for the measurement of DNP enhancement as a function of mm-wave frequency to obtain a DNP frequency profile. The gyrotron output is connected to the DNP probe via a corrugated waveguide as in most conventional MAS-DNP setups. This strategy has also been used in the context of liquid-state Overhauser DNP by Prisner and coworkers[45] and by Bennati and coworkers.[46]

We used the same microdiamond sample by Element 6 as in Ref. [30], which has a nitrogen concentration of 110-130 ppm and a particle size of 15-25 µm. A spin counting experiment at X-band showed a P1 concentration of 70 ppm (corresponding to 20 mM inside the microdiamond). Despite the relatively low mm-wave power of ~1 W at the gyrotron output in the current iteration of the gyrotron tube, we obtained ^{13}C on/off enhancements exceeding ~700 at RT and >100 at ULT. Comparison between experimental and simulated DNP profiles show that the clustering of P1 centers is at the origin of the efficient DNP observed here.

Results and discussion

DNP hardware and operation

The DNP system consists of a JEOL 600 MHz wide-bore magnet at 14.1 T, a helium gas heat exchanger using three cryocoolers, a cold He gas manifold, a MAS NMR probe for DNP experiments under ULT conditions, as described by Li *et al,*[47] and a frequency-tunable gyrotron, as described in more detail below (see Figure 1b-d). The probe is cooled by cold He gas flow that also drives bearing and spinning for MAS operation, which is cooled by a heat exchanger located next to the magnet. The exhaust He gas is recirculated into the heat exchanger in a closed cycle. The probe is equipped with a top-loading station that allows for sample exchange without warming up and removing the probe, even during operations at cold temperatures. To perform DNP experiments at ULT, the heat exchanger is cooled one day prior to commencing experiments. Cooling the NMR probe starting at RT using the closed-cycle helium MAS system connected to the heat exchanger takes about 2 hours. Sample insertion or exchange using the top-loading system is done in 15 minutes. Turning on the gyrotron and stabilizing its cavity temperature takes about 1 hour before starting experiments. Each DNP profile point requires about 8 minutes: 5 minutes for temperature stabilization of the gyrotron cavity and 3 minutes for NMR spectrum acquisition. The use of a variable-frequency gyrotron rather than variable-field magnetic field (as in conventional MAS-DNP setups) removes the need to retune the probe at each frequency, allowing for seamless frequency stepping and DNP profile capture. Still, the acquisition of a full DNP profile with this setup takes one workday given the total overhead time required for each frequency, with a typical frequency step size of 10 MHz to resolve the fine features of the experimental DNP profile.

Frequency-tunable gyrotron

The gyrotron uses second harmonic generation with a magnetic field of 7 T. The frequency of the gyrotron is tuned by adjusting the cavity temperature within a range of 10°C to 67.5°C via the cavity coolant. The optimal mm-wave frequency and power is achieved by optimizing a combination of gyrotron parameters, including the beam voltage, beam current, and the main (superconducting magnet) and the gun trim magnetic field values. Figure 2 shows the measured output power and frequency as a function of the cavity coolant temperature for a cathode voltage of 23.6 kV and a fixed magnetic field. Varying the cavity temperature between 10°C to 67.5°C, a smooth frequency tuning range of 260 MHz from 395.15 GHz to 395.41 GHz was achieved, corresponding to a rate of ~5 MHz/°C, while maintaining the output power between 0.8 and 1.2 W (note that the highest frequency points are missing on Figure 2 but are reported

in more detail in Figure S2). A broader frequency tuning range of about 800 MHz can be attained by lowering the cathode voltage, but this significantly reduces the achievable mm-wave power, down to about 0.2 W.

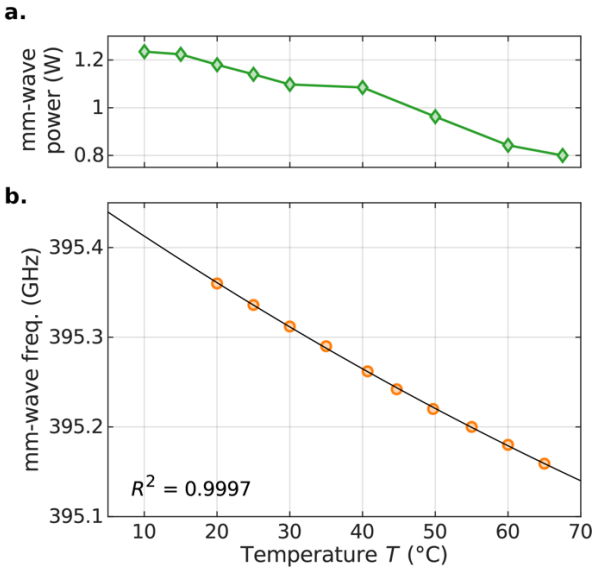

Figure 2: **a.** mm-wave frequency and **b.** power were measured while varying the cavity coolant temperature, keeping all other parameters constant. mm-wave power was recorded directly 1 m from the gyrotron cavity output. mm-wave frequency was measured by placing a mirror 1 m away from the gyrotron cavity output, reflecting at a 45° angle, and positioning the frequency measurement system (FMS) 25.4 cm away from the mirror. The black line is a quadratic regression of the mm-wave frequency with respect to the cavity coolant temperature (more details in the Supporting Information).

The relation between the mm-wave frequency and the cavity temperature was found to be approximately linear (see Figure S2). However, a closer fit is obtained when using a second order polynomial (see Figures 2b and S2). We also observed that the relation between the mm-wave frequency and the cavity temperature was subject to evolution over time (see Figure S2). In our current setup, the mm-wave frequency is measured by replacing a section of the waveguide with a mirror to divert the mm-wave beam to a frequency measurement device (see the Methods section). To ensure a sufficient resolution of the frequency during the acquisition of DNP profiles, the mm-wave frequency was measured at the beginning and the end of each DNP profile, and at several intermediate points (typically every 5°C or 25 MHz). The quadratic fit of Figure 2b was found to predict the frequency of the resulting dataset with a root mean square error of 2.7 MHz (see Figure S3). While mm-wave frequency fluctuations occur due to sensitivity to slight changes in proportional-integral-derivative (PID)-controlled parameters, such as beam current and cavity temperature, the fluctuations are minor and do not distort the broad DNP features discussed in the later sections. Furthermore, the beam current (and thus indirectly, the output power) was held stable to about 0.3 % by the PID controller in the gyrotron control system. Details on the instrumentation setup for mm-wave frequency and power measurements are provided in the Methods section and SI Section 1e.

As a comparison, the gyrotron used by Prisner and coworkers for liquid-state Overhauser DNP at 9.4 T (~260 GHz) outputs microwave at 20 W over 60 MHz, where the frequency is tuned solely via the cavity temperature.[45] The gyrotron used by Bennati and coworkers in similar conditions outputs microwaves at

~10–50 W over a range of 200 MHz and at ~10 W over a range of 500 MHz. Here, the frequency is tuned by adjusting both the cavity temperature and the cathode voltage.[46] In liquid-state Overhauser DNP experiments, the requirements for the microwaves are slightly different than for solid-state DNP. Indeed, it is necessary to achieve highly stable microwave frequency as the EPR resonance is narrower than in the solid state, but the frequency does not need to be stepped as DNP profiles in the liquid state do not usually bring useful information. The gyrotron used by Barnes and coworkers for MAS-DNP at 7 T (~197 GHz) allows for a tuning range of 335 MHz but the power varies by an order of magnitude on this range (from 10 to 110 W). In this case, the frequency is controlled with µs time-resolution via the anode voltage of the gyrotron.[43] The gyrotron used by Fujiwara and coworkers for MAS-DNP at 14.1 T outputs mm-wave over a range of 1 GHz with the frequency being controlled via the gyrotron magnetic field.[41] Again, this strategy results in a strong variation of the power over the tuning range (~9–35 W).

The gyrotron presented in this study outputs mm-waves at 0.8–1.2 W over a range of 260 MHz and to 0.2 W over a range of 800 MHz. Our aim is to increase the frequency tunability to reach the frequency separation between the DNP optima for AMUpol at 14 T, which is about ~1 GHz.[48] The performance and operation reported in this study is that of the first generation gyrotron tube that was built and adjusted over time.

DNP measurements

DNP profiles were measured as on/off ^{13}C signal enhancement in the microdiamond as a function of continuous wave mm-wave irradiation, with the mm-wave frequency stepped between 395.15 and 395.41 GHz at RT, 100 K, and 35 K under MAS at 6 kHz (see Figure 3a). The irradiation time was set to τ = 60 s, and the delay between scans set to 60 s for both the mm-wave-on and -off experiments. This value of τ was chosen to achieve practical experimental times which allows for a DNP profile of one sample to be acquired within one day.

At RT under MAS at 6 kHz, the DNP profile of the HPHT diamond displays two distinct features: a positive enhancement peak at 395.20 GHz and a negative enhancement peak at 395.37 GHz (see Fig. 3a). These peaks are ~162 MHz apart, which is different from the ^{13}C Larmor frequency of 150.9 MHz at 14.1 T. The enhancement values at the optima are listed in Table 1 and the enhancement exceeds -710 for the negative optimum. The DNP profiles measured at 100 K and 35 K (see Fig. 2a) are broader than that at RT, with the positive and negative enhancement peaks separated by ~215 MHz. Notably, the measured DNP enhancements at 100 and 35 K are lower than at RT for both the positive and negative optima (see Table 1).

At first sight, the DNP profiles in Fig. 3 have a shape expected for CE or non-resolved SE. An EPR profile at RT simulated using EasySpin is shown in Fig 3a for comparison as a gray line (see the Methods section for details on the EPR parameters). The three lines of the EPR spectrum are separated by ~90 MHz, a value that is distinct from the ^{13}C Larmor frequency (150.9 MHz). This makes the qualitative interpretation of the DNP mechanism difficult, and we hence will model the DNP profiles next. We note that the features of the DNP profiles as seen in Figure 3 were observed with other HPHT microdiamonds from different sources (Hyperion, see Figure S5).

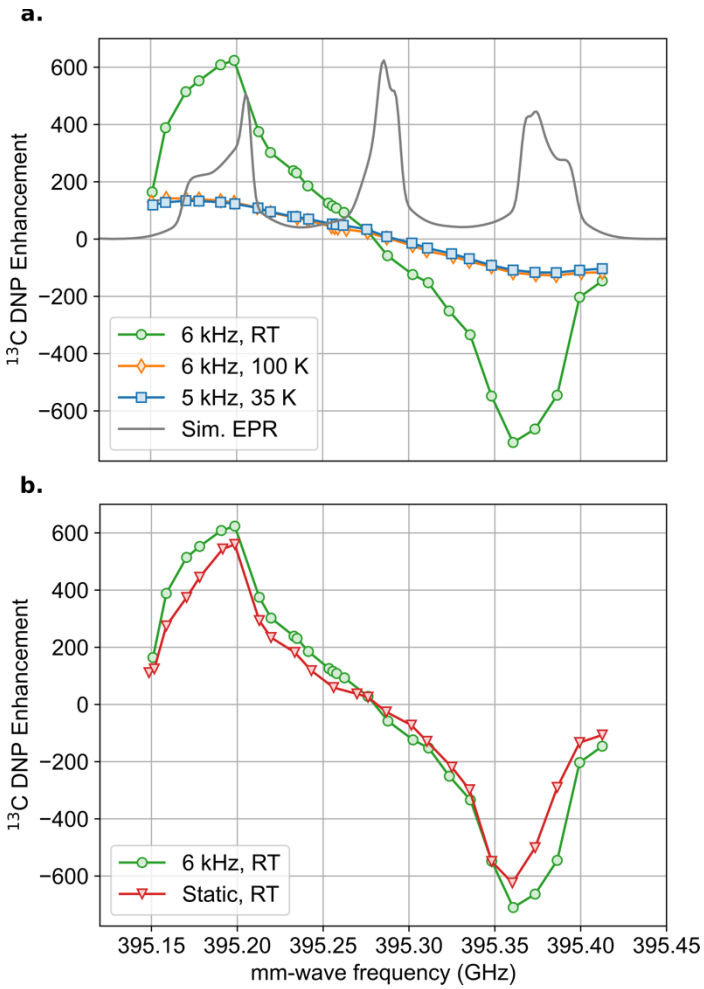

Figure 3: DNP frequency profiles of Element 6 HPHT microdiamond with a nitrogen concentration of 110-130 ppm. The figure demonstrates (a) the effect of temperature under MAS and (b) the effect of MAS at RT. The ^{13}C DNP frequency profiles were obtained by measuring signal enhancements after 60 s as a function of irradiation frequency swept from 395.15 GHz to 395.41 GHz with 0.8–1.2 W output power. The simulated EPR profile (grey) shown in (a) was simulated based on RT data of a similar diamond taken at 13.8 T (see the Methods section for details).

Table 1: ^{13}C signal enhancement in Element 6 HPHT microdiamond at different temperatures, expressed as on/off enhancement after τ = 60 s of mm-wave irradiation (defined in Eq. 7) for the positive and negative DNP optima (indicated as + and – lobes, respectively). The RT results are also expressed in terms of absolute enhancement at 60 s and infinity (defined in the Sample and Methods section, Eq. 8).

T (K)	DNP lobe	$\omega_{mw}/2\pi$ (GHz)	$\varepsilon_{on/off}(60)$	$\varepsilon(60)$	$\varepsilon(\infty)$
298 (static)	+	395.199	+560	N.A.	N.A.
	–	395.360	-624	N.A.	N.A.
298 (MAS)	+	395.199	+624	58	255
	–	395.361	-710	-67	-259
100	+	395.171	+142	N.A.	N.A.
	–	395.386	-127	N.A.	N.A.
35	+	395.171	+134	N.A.	N.A.
	–	395.386	-117	N.A.	N.A.

As mentioned above, the DNP profiles were acquired with τ = 60 s for both mm-wave-off and -on experiments. This delay is much shorter than the ^{13}C spin-lattice relaxation time (T_1) of ~ 10 min (see SI), and hence the enhancements reported in Figure 3 correspond to $\varepsilon_{on/off}(60)$, which is different from the absolute enhancement $\varepsilon(60)$ (see the definitions in Eqs. 7 and 8, respectively). We measured both the nuclear T_1 and the DNP build-up time constant (T_{DNP}) at RT under MAS. This allowed us to determine the absolute enhancement after 60 s and at infinite time to be about 60 and 250, respectively (see Table 1). We did not measure the T_{DNP} values at lower temperature and hence, cannot report on the absolute enhancements at ULT. We chose to present all DNP spectra as $\varepsilon_{on/off}(60)$ so that they are comparable.

EPR lineshape analysis

The interpretation of the DNP profiles requires a precise knowledge of the EPR line of the PA. In the case of P1 centers, the EPR line contains three peaks corresponding to the projections of the coupled ^{14}N nuclear spin. We have recently shown that a significant portion of P1 spins were clustered giving rise to a non-vanishing intensity in between the three lines.[30] In the same study, we found that the nutation frequency of these clustered spins was larger than that of isolated spins, giving a clear indication of exchange coupling or exchange coupling among the clustered spins. Another study published at the same time on HPHT diamonds also evidenced the presence of P1 clusters with exchange couplings.[31] In the latter study, the P1 EPR line of a single crystal HPHT diamond at 13.8 T was fitted by the sum of three contributions: isolated P1 spins, dipolar broadened spin, and exchange-coupled spin pairs. The isolated and dipolar broadened spins were fitted with the same EPR parameters except for the linewidth. The exchange coupling in the spin pairs was fitted to an approximate value of $J/2\pi$ = 139 MHz.[31]

In all DNP simulations presented in the next sections, we used the EPR parameters reported in Ref. [31]: g-factors $g_\parallel$ = 2.00218 and $g_\perp$ = 2.00220; P1-^{14}N hyperfine interaction values $A_\parallel/2\pi$ = 114.0 MHz and $A_\perp/2\pi$ = 81.3 MHz; ^{14}N quadrupolar constant $P_\parallel/2\pi$ = -3.97 MHz; $J/2\pi$ = 138.7 MHz for exchange-coupled spins; Gaussian line broadening of 5, 30 and 17.5 MHz for isolated P1 spins, dipolar-broadened P1 spins and exchange-coupled P1 pairs, respectively. The relative contributions of the isolated, dipolar-broadened, and exchange-coupled P1 spins to the overall EPR line are 0.49, 0.38, and 0.13, respectively. The resulting EPR line is shown as a grey line in Figure 3a (Figure S7 shows the spectral contribution of each population). Note that the values of the hyperfine and quadrupolar interactions were originally reported from Ref. [49]. We note that in Ref. [30], we obtained slightly higher values for the P1 g-tensor ($g_\parallel$ = 2.00225 and $g_\perp$ = 2.0023) than those of Ref. [31]—we chose the latter values in this study. We made this choice because the values from Ref. [31] were obtained from experimental data at higher magnetic field than the values in Ref. [30] (13.8 compared to 8.2 T), which should lead to a more precise measurement of the g-tensor. This expectation is further validated with the lower values in Ref. [31] yielding an EPR line that aligns better with our experimental DNP profiles.

1 electron-1 nucleus and 2 eletron-1 nucleus DNP models

To understand the DNP mechanisms at play in the diamond sample studied here, we first use a simple analytical model. In this model, the DNP profile corresponding to each mechanism is computed as a convolution of the EPR line with a function that is specific to each mechanism (see below). The overall DNP profile is obtained by the weighed sum of the contributions of the different mechanisms. The comparison between the experimental DNP profiles and the simulation for a particular mechanism was then used to assess whether the mechanism can describe the experimental data. Similar models have been presented in previous studies on DNP of microdiamonds by Bretschneider *et al*.[26] at 3.3 T and 1.65 K

in static mode, by Shimon *et al.*[28,29] and by Bussandri *et al*.[30] at 3.3 and 7 T at RT in static mode. Using a similar approach, we show at 14.1 T that DNP mechanisms that rely on one or two electron spins cannot reproduce any of the DNP spectral features shown in Figure 3, but that DNP mechanisms involving clusters of strongly coupled spins can.

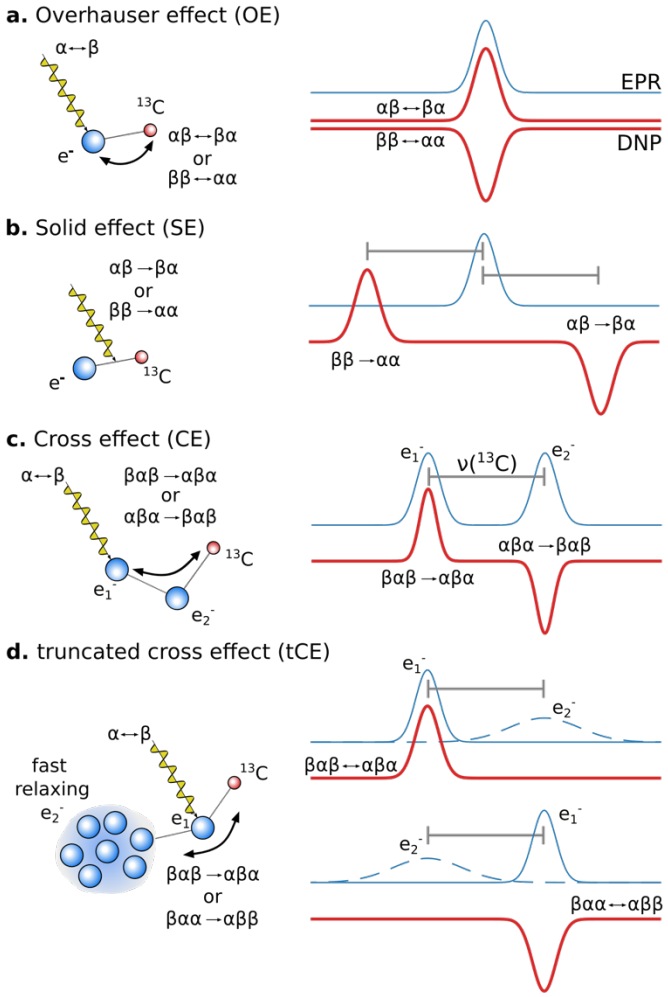

Figure 4: Schematic representation of the DNP mechanisms without spectral diffusion. Yellow arrows represent mm-wave saturation. Black arrows represent spontaneous flip-flops or triple spin flips. Horizontal grey lines on the EPR spectra and DNP profiles represent the ^{13}C Larmor frequency. **a**. In OE, a single quantum transition is saturated and polarization transfers spontaneously to the nuclear spin by a zero (or double) quantum transition, resulting in negative (or positive) DNP. **b**. In SE, mm-waves drive a double-quantum (or zero-quantum) transition involving one nucleus and one electron, resulting in positive (or negative) DNP. **c**. For CE, mm-waves saturate the single-quantum transition of electron e_1^- (or e_2^-), with $|\omega_0(^{13}C)| = |\omega_0(e_1^-) - \omega_0(e_2^-)|$. A triple-spin flip involving two electrons and one nucleus subsequently flips the nucleus, leading to positive (or negative) DNP. **d**. tCE is like the CE except that e_2^- relaxes faster than e_1^-, which makes it inefficiently saturated by mm-waves, resulting in a DNP profile with a single lobe. The state labels correspond to e^-–^{13}C and e_1^-–e_2^-–^{13}C spins systems in the two and three spin cases, respectively, with α and β representing the spin being aligned parallel and antiparallel with the magnetic field, respectively. The transition indicated in the DNP profile correspond to DQ or ZQ saturation (a), DQ or ZQ cross-relaxation (b), and triple-spin flips (c,d).

We first consider the Overhauser effect (OE) as a possible mechanism. OE is induced by saturating the allowed single-quantum EPR transition (see Figure 4a). Nuclear polarization subsequently builds up due to an imbalance between zero-quantum and double-quantum cross-relaxation rates, which requires modulation of the hyperfine interaction near the electron Larmor frequency.[50] Such modulations have been proposed to give rise to OE at low temperatures in semiconductors[51] and in π-conjugated networks,[52–54] but are not expected to occur in an insulating rigid diamond lattice.[26,30,31] Moreover, an OE mechanism should give rise to a DNP profile with a similar shape as the EPR line itself, which does not match experimental observation.

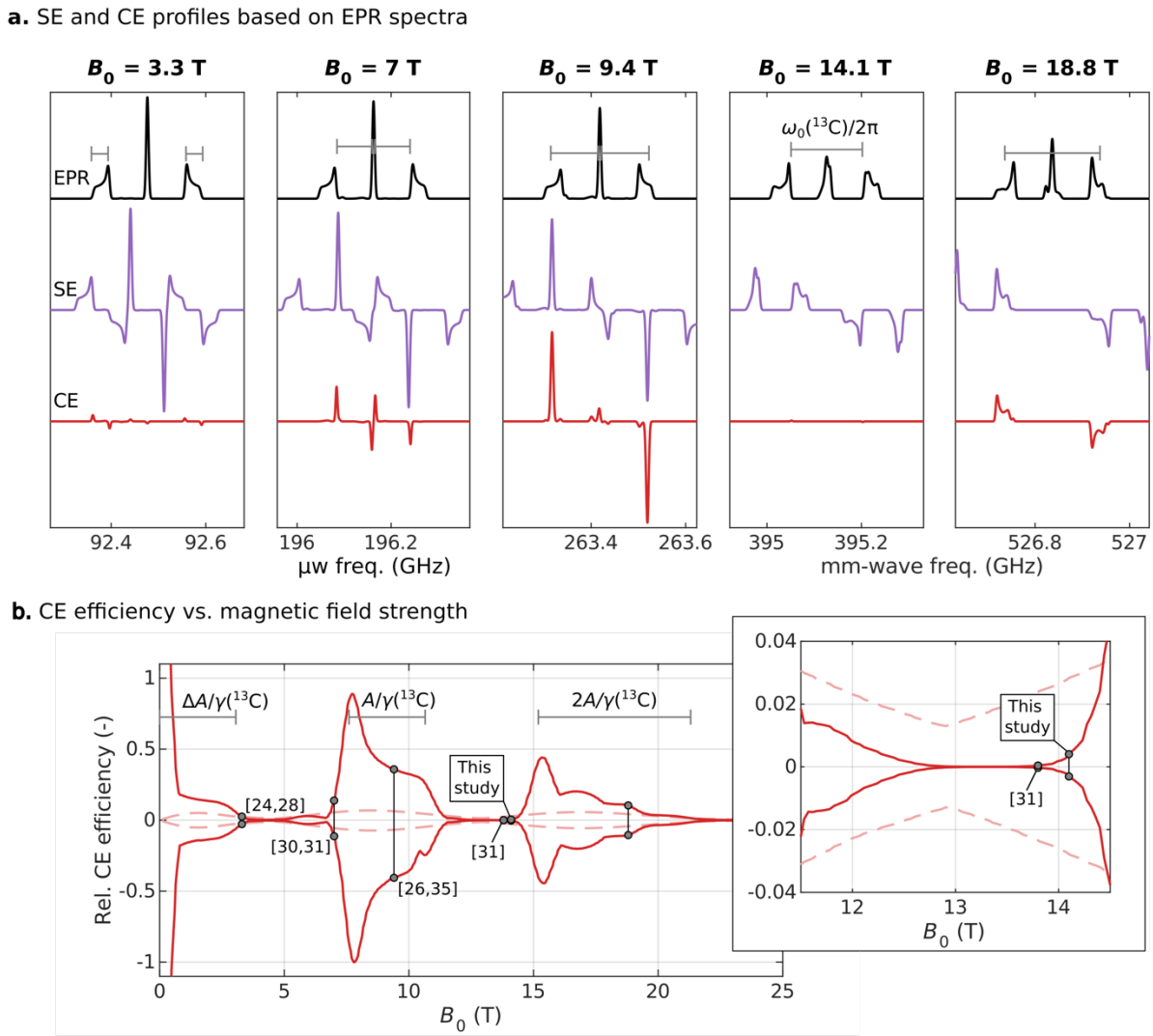

Figure 5: **a**. Comparison of the simulated EPR line for isolated P1 spins and theoretical DNP profiles for SE and CE at various magnetic fields, showing that CE is almost nonexistent at B_0 = 14.1 T, *i.e.* the magnetic field used in this work. The grey horizontal lines represent the ^{13}C Larmor frequency. All four SE profiles are normalized with respect to the most intense SE value (obtained for B_0 = 3.3 T). All four CE profiles are normalized with respect to the most intense CE value (obtained for B_0 = 9.4 T). **b**. Efficiency of the CE mechanism as a function of magnetic field for both positive and negative DNP, relative to the negative enhancement at 7.8 T. The solid and faint dashed red lines represents the CE efficiency computed using the EPR line of the narrow-line P1 centers only (as shown in panel a) and using that of the dipolar-broadened populations, respectively. The black dots indicate the value of the five magnetic field strengths

represented in panel a, with the corresponding references to published work. The horizontal grey lines indicate the magnetic field values of the three matching conditions, where the Larmor frequency of ^{13}C spins is smaller than the anisotropy of the hyperfine interaction ΔA; equal to the hyperfine interaction A; and equal to the twice the hyperfine interaction $2A$. The inset shows a zoom around the magnetic field used in this work. The SE and CE DNP profiles are computed using Eqs. S19 and S32, respectively.

Next, we test the effect of SE DNP. SE is obtained by saturating the low-probability zero-quantum or double-quantum electron-nuclear transitions (see Figure 4b).[55] The SE DNP profile is computed from the difference between two copies of the EPR line shifted by $-\omega_0(^{13}C)$ and $+\omega_0(^{13}C)$. In the simulated SE DNP profile, the separation between the positive and negative optima is 126 MHz (see Figure 5a). The experimental DNP profiles show a frequency separation between 165 to 220 MHz, hence not matching the SE DNP profile. Furthermore, saturating zero- and double-quantum transitions requires strong mm-wave power, especially at high magnetic fields, and should not be efficient in our conditions of modest (~1 W) mm-wave power at 14.1 T. The SE is therefore not the dominant contributor to our experimental observations.

CE is often the dominating mechanism in MAS-DNP.[56,57] As with OE, CE-DNP starts by the saturation of an allowed single-quantum EPR transition but requires a second electron whose polarization is (ideally) unaffected by the mm-waves (see Figure 4c). The polarization difference between the two electrons then transfers spontaneously to the ^{13}C spin if the three spins fulfill the CE matching condition $|\omega_0(^{13}C)| = |\omega_0(e_1^-) - \omega_0(e_2^-)|$, ($\omega_0(^{13}C)$ and $\omega_0(e_k^-)$ being the Larmor frequency of the ^{13}C spin and of the k^{th} electron spin, respectively). The CE therefore requires the presence of electron spin pairs whose Larmor frequency difference matches the nuclear Larmor frequency. The CE profile can be computed as the product of the EPR line and the predicted SE DNP profile.[28,58] We note that this simple model assumes that electron spectral diffusion is negligible and that the electronic T_{1e} is homogeneous across the EPR line (see SI for a detailed derivation). Furthermore, this model does not account for MAS but, as the DNP profiles at RT for the MAS and static case are almost identical in shape, we do not expect MAS to significantly modify the DNP mechanism. Figure 5a shows the simulated EPR line of isolated P1 spins and the corresponding SE and CE profiles for a series of values of the magnetic field strength, including the result presented in this work at 14.1 T. Because the CE profile is given by the product of the SE profile and the EPR line, it has non-zero amplitudes only where the two overlap. Figure 5a shows that there is little overlap between the EPR line and the SE profile at 14.1 T, suggesting the effect of CE among the isolated P1 spins is negligible.

To get a clearer view of the conditions where CE is expected to be efficient, the CE profile was computed as in Figure 5a, for an array of magnetic field values between 0.1 and 25 T. Figure 5b shows the predicted maximum positive and negative CE enhancements as a function of the magnetic field strength as a solid red line. Three distinct regimes where CE is efficient may be identified.[26,31] First, at field such at 3.3 T and less, the nuclear Larmor frequency $\omega_0(^{13}C)$ is smaller than the hyperfine anisotropy $\Delta A = A_\parallel - A_\perp$ and so a pair of electrons fulfilling the CE matching condition may be found within one of the external lines of the EPR spectrum. Second, at a higher field regime of 7 or 9.4 T the $\omega_0(^{13}C)$ values lie between the $A_\parallel$ and $A_\perp$ hyperfine coupling constants. Therefore, one electron in the central EPR line may fulfill the CE matching condition together with another electron corresponding to one of the external EPR lines. Finally, in the regime at the highest field considered here at 18.8 T, $\omega_0(^{13}C)$ lies between $2A_\perp$ and $2A_\parallel$. Therefore, one electron in each of the external EPR lines matches the CE condition. Because 14.1 T is not part of any of these regimes, CE is inefficient with narrow-line isolated P1 centers at this particular field. As clustering broadens the EPR line, coupled P1 spins are expected to better fulfill the CE matching conditions. To verify

this, the CE efficiency as a function of the magnetic field strength was computed for the population of dipolar-broadened spins[30,31] alone with the dipolar coupling strength taken from Ref.[31] of HPHT diamond as discussed earlier (dashed faint red lines in Figure 5b). The broadening of the EPR line results in a broadening of the matching conditions, resulting in a more even CE efficiency across different fields but lower maximum values, because the broadening dilutes the contributions of spins that fulfilled CE without broadening. At 14.1 T, the CE efficiency is improved by a factor ~7 for dipolar-broadened P1 spins compared to isolated P1 spins, but still corresponds to only 3% of the efficiency at the optimal field, i.e., 7.8 T.

DNP mechanisms involving clustered spins

We turn to the truncated CE (tCE) as a likely dominant mechanism. tCE is a form of CE where the two electron spin partners fulfilling the CE condition differ in relaxation rate. The slow-relaxing electron spin is first saturated by mm-wave irradiation and then undergoes a triple-spin flip with the nuclear spin and the fast-relaxing electron spin partner (see Figure 4d). Because of fast relaxation, the latter rapidly returns to equilibrium and is ready to undergo a new triple spin flip. tCE is optimal when the slow- and fast-relaxing populations are separated by the nuclear Larmor frequency, as depicted in Figure 4d. The effect is said to be "truncated" because it is only efficient when the slow-relaxing spins are saturated and undergo triple spin flip with a fast-relaxing electron spin meeting the CE condition, but not when irradiating the fast-relaxing spins. In the latter case, even when they fulfill the CE condition with a slow-relaxing electron spin, the fast-relaxing spins return to equilibrium before they can polarize the nuclear spins via a triple-spin flip process. In the simple case shown in Figure 4d, this gives rise to a single lobe absorptive DNP profile that has the shape of the EPR line of the slow-relaxing spins (note that this spectral feature is not a priori distinguishable from OE). tCE will gives rise to a positive or negative absorptive DNP profile depending on whether the fast-relaxing spins have a higher or lower resonance frequency, respectively, relative to the slow-relaxing spins (see Figure 4d).

Figure 6a shows the experimental normalized DNP profiles together with simulated profiles (colored symbols and black line, respectively), obtained as a linear combination of CE and tCE. The tCE and CE components making up the simulated DNP profiles that closely describe the experimental profile show that tCE is the dominant contributor. For tCE, the dipolar-broadened and isolated P1 spins that make up the observable EPR spectrum were assumed to play the role of slow-relaxing spins, while the exchange-coupled P1 spins play the role of fast-relaxing spins. The simulated EPR spectrum of the slow- and fast-relaxing components (Figure 6b-c) show the dramatic differences in their broadening, and the fast-relaxing spectral component spanning well beyond the entire visible EPR spectrum. CE is assumed to occur only among the slow-relaxing spins, i.e. isolated or dipolar broadened. The simulated tCE profiles feature larger separations between the positive and negative DNP optima than the simulated CE (and SE) profiles, which are closer to the experimental values (see Table S3). Three points were key to obtain a good fit of the model to the experimental data: first, spectral diffusion was assumed to spread the effect of mm-wave saturation among the slow-relaxing spins and modeled phenomenologically; second, the EPR spectrum of the exchange-coupled spin pairs was simulated while accounting for the high electron polarization at low temperatures; finally, a dipolar coupling of 50 MHz was assumed between the exchange-coupled spins (which was not included in the fit reported in Ref. [31]). These three points are detailed in the following sections.

The enhancement from CE was computed using Vega and coworkers' indirect CE (iCE) formula[59]

$$f_{\mathrm{CE}}(\omega_{\mathrm{mw}}) = \sum_k f_{\mathrm{S}}(\omega_k) f_{\mathrm{S}}(\omega_k + \omega_{\mathrm{I}}) \frac{P_{\mathrm{S}}^{\mathrm{mw}}(\omega_k) - P_{\mathrm{S}}^{\mathrm{mw}}(\omega_k + \omega_{\mathrm{I}})}{1 - P_{\mathrm{S}}^{\mathrm{mw}}(\omega_k) P_{\mathrm{S}}^{\mathrm{mw}}(\omega_k + \omega_{\mathrm{I}})},$$ Eq. 1

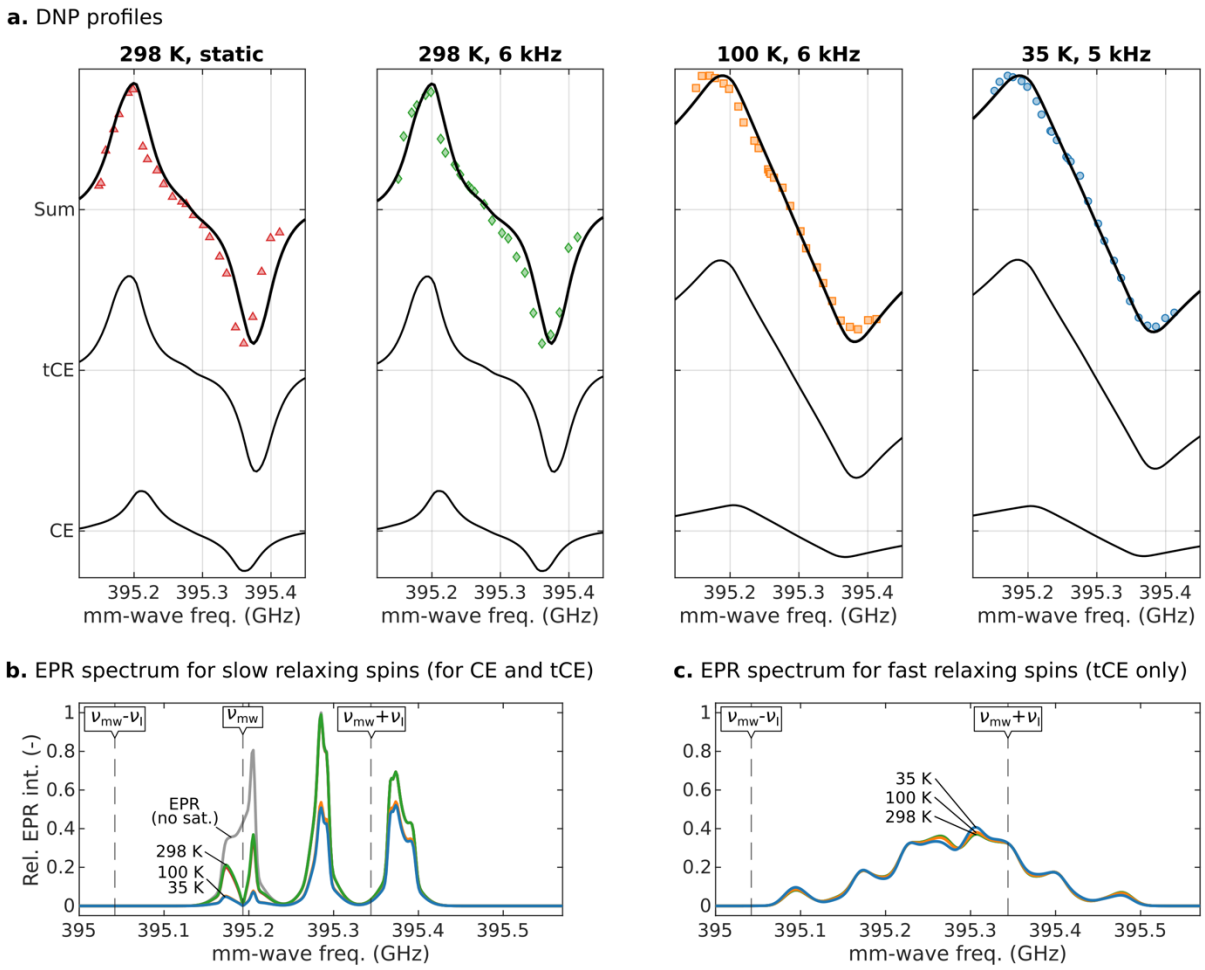

Figure 6: **a**. Comparison of the experimental DNP profiles (colored symbols) with the model of combined CE and tCE (black lines) presented in Eqs. 1 and 2, where isolated and *D*-broadened spins play the role of slow-relaxing partners, and exchange-coupled pairs play the role of fast-relaxing partners. The slow-relaxing spins are efficiently saturated by mm-wave irradiation while the fast-relaxing spins are assumed to always be at thermal equilibrium with polarization P_0. **b**. Simulated EPR line of the slow-relaxing P1s spins (isolated and *D*-broadened) at thermal equilibrium (in grey) and under mm-wave saturation (colored lines) on resonance with the low frequency EPR peak (shown as an example), with $\nu_{mw} = \omega_{mw}/2\pi$. The effect of spectral diffusion and electron spin-lattice relaxation during saturation is modeled using Eq. 3. At lower temperature, T_{1e} gets longer allowing the effect of saturation to spread on a larger range of frequencies (see Eqs. 3 and 4). **c**. EPR line of the fast-relaxing exchange-coupled P1 pairs, whose line shape becomes asymmetric at low temperature due to high polarization, with $\nu_I = \omega_I/2\pi$ being the nuclear Larmor frequency. The stronger EPR intensity of the fast relaxing-spins at $\nu_{mw} + \nu_I$ (in panel b) relative to that of the slow-relaxing spins (in panel c) is consistent with tCE being more efficient than the CE (see panel a).

which accounts for triple spin flips between all spin pairs fulfilling the CE matching condition, not only those on resonance with the mm-wave irradiation. $f_S(\omega)$ is the EPR intensity (or density of states) at frequency ω, $P_S^{mw}(\omega)$ is the polarization of the slow-relaxing spins at frequency ω under saturation at

frequency ω_{mw}, and ω_I is the nuclear Larmor frequency. The product $f_S(\omega_k)f_S(\omega_k + \omega_I)$ is proportional to the probability for a pair of slow-relaxing spins to fulfill the CE matching condition. If spectral diffusion is negligible, the EPR line is only modified by the mm-wave irradiation on resonance with it. Hence, $P_S^{mw}(\omega_k)$ is only different from P_0 for $\omega_k = \omega_{mw}$, and the polarization difference $P_S^{mw}(\omega_k) - P_S^{mw}(\omega_k + \omega_I)$ is only non-zero for $\omega_k = \omega_{mw}$. In this case, the sum in Eq. 1 simplifies to a single non-zero element, which corresponds to direct CE.[59] The sum over frequencies ω_k combines the effect of all pairs fulfilling the CE matching conditions for a given value of ω_{mw}. The denominator is a normalization factor that only plays a role when the electron polarization approaches unity.

The enhancement due to the tCE was computed adapting Eq. 1 to the case of triple spin flips between slow- and fast-relaxing spins (see Section 3 of the SI for a detailed derivation),

$$f_{tCE}(\omega_{mw}) = \sum_k \left(f_S(\omega_k) f_F(\omega_k - \omega_I) \frac{P_0 - P_S^{mw}(\omega_k)}{1 - P_0 P_S^{mw}(\omega_k)} + f_S(\omega_k) f_F(\omega_k + \omega_I) \frac{P_S^{mw}(\omega_k) - P_0}{1 - P_0 P_S^{mw}(\omega_k)} \right). \quad \text{Eq. 2}$$

Here, f_S and f_F are the EPR intensities (or density of states) of the slow- and fast-relaxing spins, respectively. The products $f_S(\omega_k)f_F(\omega_k + \omega_I)$ and $f_S(\omega_k)f_F(\omega_k - \omega_I)$ are proportional to the probabilities for a pair of slow- and fast-relaxing spins to fulfill the CE matching condition, where the slow-relaxing spins have frequency ω_k. $P_S^{mw}(\omega_k)$ and P_0 are the polarizations of the slow-relaxing spins at equilibrium under mm-wave irradiation at frequency ω_{mw} and that of the fast-relaxing spins, which is assumed to be constant and equal to the Boltzmann equilibrium value due to the hypothesis of fast-relaxation. The difference in polarization between the slow- and fast-relaxing P1 spins is transferred to nearby nuclear spins by triple spin flips. Note the difference in sign in the polarization difference $P_0 - P_S^{mw}(\omega_k)$ between the left and right terms in Eq. 2, which leads to DNP of opposite signs.

We tested two approaches to model spectral diffusion among the slow-relaxing spins. An analytical solution[60] to the spectral diffusion equation proposed by Wenckebach[61] and Vega's electron spectral diffusion (eSD) model.[59,62–64] Both models describe the electron spin polarization as a function of frequency in the EPR line, under the influence of mm-wave irradiation, T_{1e} relaxation, and electron-electron flip-flops. They should be seen as phenomenological as they were developed for static conditions and do not account for MAS. They gave similar results although the analytical model results in a slightly better fit to the experimental data. The two models are detailed in the SI (Section 4) and the resulting simulated DNP profiles are compared. Here, we only show the analytical model, which was used in Figure 6. In this model, the steady-state electron polarization across the EPR line is the solution to the spectral diffusion equation, which follows an exponential law[60]

$$P_S^{mw}(\omega_k) = P_0 \left(1 - \exp\left(-\frac{|\omega_k - \omega_{mw}|}{\Lambda}\right)\right), \quad \text{Eq. 3}$$

where ω_{mw} is the mm-wave irradiation frequency, and Λ the spectral diffusion length, defined as

$$\Lambda = \sqrt{T_{1e} D}, \quad \text{Eq. 4}$$

where T_{1e} is the electron spin-lattice relaxation time constant and D the spectral diffusion coefficient. In analogy to the diffusion length in Fick's law, Λ expresses how far in the EPR spectrum the effect of the mm-wave irradiation propagates under the competing influence of spectral diffusion and relaxation. D depends on the strength of the spin-spin interaction and can be expected to be independent of temperature. In contrast, T_{1e} increases with decreasing temperature, which implies that the spectral diffusion length can vary with temperature. Hence, the lower the temperature, the further spectral diffusion spreads the effect

of saturation. The EPR line under mm-wave saturation is shown as colored lines in Figure 6b. It is obtained by taking the product of the EPR line at Boltzmann equilibrium (grey line in Figure 6b) with the polarization as predicted by Eq. 3. The values of the spectral diffusion length and the saturation factors were fitted manually at the three temperatures and reported in Table 2.

The electron polarization at 14.1 T and low temperatures breaks the high temperature approximation (see Table 2). Hence, the EPR line of coupled spins depends on electron polarization and in turn on temperature (see Figure 6b). Indeed, at 35 K, with P_0 = 0.26, a P1 center has a higher probability to find its coupled neighbor P1 electron spin in the β state rather than in the α state, resulting in an asymmetric EPR line. This, in turn, contributes to the imbalance between the positive and negative DNP optima observed in the experimental data (see Figure 6a); as temperature decreases, the imbalance between positive and negative lobe increases. As mentioned above, we also assumed a dipolar coupling of 50 MHz for the coupled P1 pairs, unlike in Ref. [31] where the P1 EPR line was fitted with $J/2\pi$ = 138.7 MHz and D = 0. Setting a non-zero value for D does not strongly change the appearance of the EPR line whose shape is dominated by isolated, narrow-line, P1 centers. However, it does affect the simulated DNP profile (note that it is reasonable to assume that spins with a large echange coupling will also feature dipolar couplings). The value of D was obtained as a rough fit. We note that the interplay between J and D changes the shape of the EPR line at high electron polarization. However, both these values are difficult to determine with precision.[31,35]

Table 2: Parameters used to compute the DNP profiles: Boltzmann electron polarization P_0 was calculated using Boltzmann equation (see Eq. S3); spectral diffusion length Λ; relative contribution of tCE to the simulated DNP profile x_{tCE}. Values of Λ and x_{tCE} were fitted manually to the experimental data.

T (K)	P_0 (-)	Λ (MHz)	x_{tCE}
298, static	0.0318	22	0.6
298, MAS		20	0.6
100	0.0946	120	0.7
35	0.265	130	0.7

The modeling of the DNP profile confirms that the spectral diffusion length increases with decreasing temperature (see Table 2), as expected (see Eq. 4). Vega's eSD (see Table S2 and Figure S8) also predicts an increase in T_{1e} with decreasing temperature from fitting the DNP profiles. Although they are phenomenological, both spectral diffusion models converge to the same conclusion, that is that the broadening of the DNP profile at low temperature is due to an increase in T_{1e}. As already mentioned (Figure 6a, Table 2), the contribution of tCE to the overall DNP profile is larger than that of CE. This makes sense given the fact that the number of P1 spins fulfilling the CE matching condition is small at 14 T (see Figures 5b and 6b).

Electron spin saturation measurements

The tCE model presented in this study is valid when there is a difference in T_{1e} between different P1 populations and consequently a change in the saturation efficiency of those populations. We verified these hypotheses by performing EPR measurements on a microdiamond sample from the same batch under similar conditions (B_0 = 13.8 T and T = 35 and 298 K) in static mode using the instrumental setup recently presented by Nir-Arad *et al.*[65,66]. The saturation efficiency of different P1 populations was measured using the pulse sequence of Figure 7a. Standard frequency-swept echo-detected EPR spectra (pulse sequence of Figure 7a without pump) were first recorded at RT and 35 K (colored lines in Figure 7b). The general

appearance of the spectra is the same, although the ratio between the isolated and exchange coupled components is altered. While the T_{1e} increases with the reduction of the temperature for all the spectral components, this reduction is the strongest for the isolated component. For the EPR spectrum acquired at 35 K, the relative intensity of the isolated component is reduced due to incomplete recovery during the pulse sequence repetition time. The EPR signal was measured again at select frequencies on resonance with the narrow peaks and in between them, but after pumping the spins at these frequencies with t_{pump} = 10 ms (see pulse sequence in Figure 7a). This experiment measures the remaining EPR signal after saturating the spins at a given frequency. The colored dots in Figure 7b show the saturation efficiency at the measured frequencies, given by

$$s = 1 - \frac{I_{sat}}{I_0}, \qquad \text{Eq. 5}$$

where I_{sat} and I_0 are the signal intensities with and without prior pumping (saturation), respectively. Both at RT and at 35 K, P1 centers are more efficiently saturated on resonance with the narrow population than the intensity in between, which originates mostly from the exchange-coupled P1 spins. The difference in saturation between narrow and broad populations is larger at RT than at 35 K. This likely explains the stronger relative DNP efficiency observed at RT compared to at cryogenic temperatures in this study (see Figure 6).

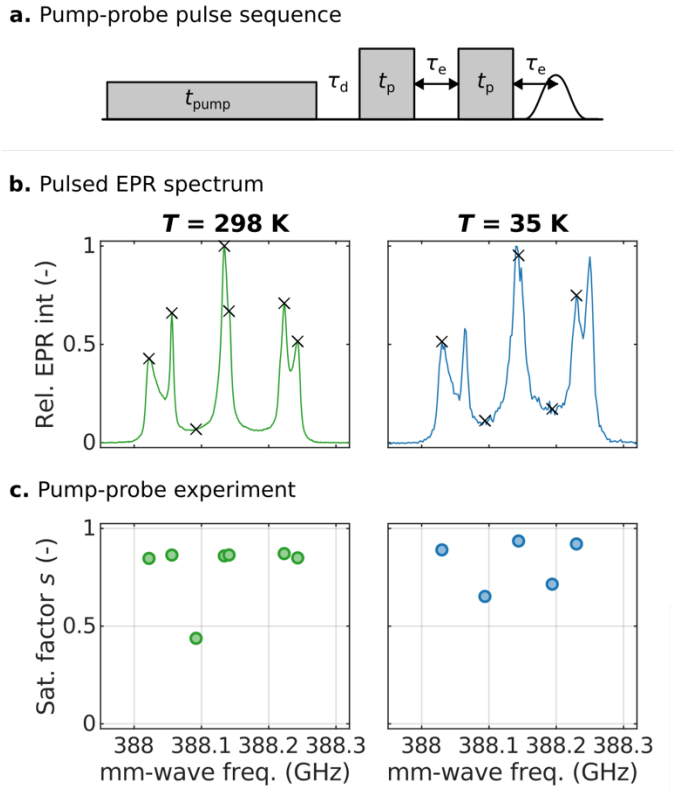

Figure 7: Efficiency of the EPR line saturation at different mm-wave irradiation frequency at RT and at 35 K, recorded at 13.8 T in static mode using a pump-probe pulsed EPR scheme, where the pump and probe pulses are set to the same frequency. **a**. Pulse sequence for pump-probe pulsed EPR experiments. t_p = probe pulse length, t_{pump} = pumping pulse length. **b**. Frequency-swept echo-detected EPR line at thermal equilibrium (without pump). **c**. Saturation efficiency at select frequencies, as defined in Eq. 5. Crosses in panel b show the positions where the pump-probe experiments were conducted.

Limitations of the DNP model

The effect of electron spin saturation and spectral diffusion in P1 centers on the DNP profile is significantly impacted by the specific experimental conditions of this study. The spectral diffusion model used here (see Eq. 3) was developed for static DNP studies[61] and is only accurate under MAS if T_{1e} is short compared to the rotor period such that the processes of saturation, spectral diffusion, and relaxation occur before a full revolution. Under MAS and at lower temperature where the T_{1e} of the P1 center is likely to be longer than the duration of one revolution, saturated electron spins do not fully relax back to Boltzmann equilibrium before the sample orientation changes. If effects of saturation outlive a rotor period, spectral diffusion within each of the three EPR transitions is enhanced as it statistically allows more electron spin pairs to be degenerate and exchange polarization. Therefore, mm-wave irradiation should affect all spins within an inhomogeneously-broadened EPR line close to evenly. All the saturated slow-relaxing spins within the EPR line can then undergo a triple spin flip with the exchange-coupled spins.

The observed DNP properties of P1 centers in HPHT diamond is strongly influenced by the field used in this study of 14.1 T. At this field, the hyperfine interaction with the ^{14}N spin is in the intermediate coupling regime, where the isotropic hyperfine constant is equal to twice the nuclear Larmor frequency (here, $A_{iso}/4\pi$ ~ 46 MHz and $\omega_0(^{14}N)/ 2\pi$ ~ 43 MHz). This leads to a significant state mixing in the m_S = +1/2 electron spin manifold, making 9 transitions per e-^{14}N system allowed and contributing to the EPR spectra. The transitions connecting different ^{14}N states provide un unusual mechanism for polarization transfer across the EPR spectrum thus contributing to eSD.[40] Figure 8a shows the energy diagrams and allowed EPR transitions for the strong, intermediate, and weak coupling regimes, corresponding to low, intermediate, and high magnetic field limits. The transition intensities for the same field regimes are shown as histograms in Figure 8b. Finally, the EPR spectra decomposed in different transitions are shown in Figure 8c. In the limits of strong and weak coupling (low and high field, respectively), only three EPR transitions are allowed. However, 14.1 T falls in-between these limits, and all nine transitions are allowed. The situation is even more complicated for P1 pairs that experience exchange coupling that is estimated to be about three times that of the ^{14}N nuclear Zeeman and hyperfine interactions.[31] The fact that these three interactions are on the same order of magnitude causes more than 200 transitions to be allowed. Figure S11 shows that the most intense transition only accounts for 5.4% of the total EPR intensity and the 20 most intense transitions together make up for still less than 50% of the total EPR line.

The findings of the present study differ from those of Ref. [30] where RT DNP was performed at 3.3 and 6.9 T on the same HPHT diamond sample as studied here. In that study, DNP profiles were found to be the sum of contributions of SE, CE, and tCE, all three with comparable intensities. The presence of significant SE at 3.3 and 7 T but not at 14.1 T can be explained by the decrease of the efficiency of SE with increasing magnetic field and possibly a stronger saturating field available at 3.3 T. The vanishingly small number of non-clustered P1 pairs fulfilling the CE matching conditions explains why 14.1 T is a special case where CE is particularly inefficient (see Figure 5). The model for tCE presented here differs from that used in Ref. [30] where the tCE profile was computed as the sum of three EPR peaks and their sign and intensity left as free fit parameters. The sign of the tCE enhancement corresponding to each of the three EPR peaks was hypothesized to come from the presence of a population of fast-relaxing spins with an asymmetric EPR line that displays greater intensity at lower frequencies. In this study, the tCE contributions were modeled using the slow- and fast relaxing EPR components and considering the effects of electron spin polarization (see above) and was shown to describe the experimental DNP profiles at 14.1 T and at different temperatures without the need to use additional fudge factors. The same physical model for the DNP

profile at 14.1 T was used to simulate the DNP profile at 3.3. and 6.9 T (shown in Figure S10). The resulting DNP profile was found to be in excellent agreement with the experimental DNP data at 6.9 T described in Ref. [30] (see Figure S10b). The model derived from this study at 14.1 T could capture the 6.9 T DNP profile data more accurately than previous models. In other words, the DNP study at 14.1 T presented here contributed to generating a more complete picture of the spectral population of P1 centers in HPHT diamond than previously known. To the contrary, the model did not fully reproduce the tCE contribution to the DNP profile at 3.3 T (see Figure S10a). It is possible that broader paramagnetic species with a lower *g*-factor than the P1 species captured by EPR plays the role of fast-relaxing spins for tCE at 3.3 T,[30] but not at higher field, possibly due to an increase in relaxation rate at higher field. This study shows that there is a myriad of "hidden" paramagnetic species that are not directly captured by EPR but are reflected in the characteristics of DNP profiles at different magnetic fields.

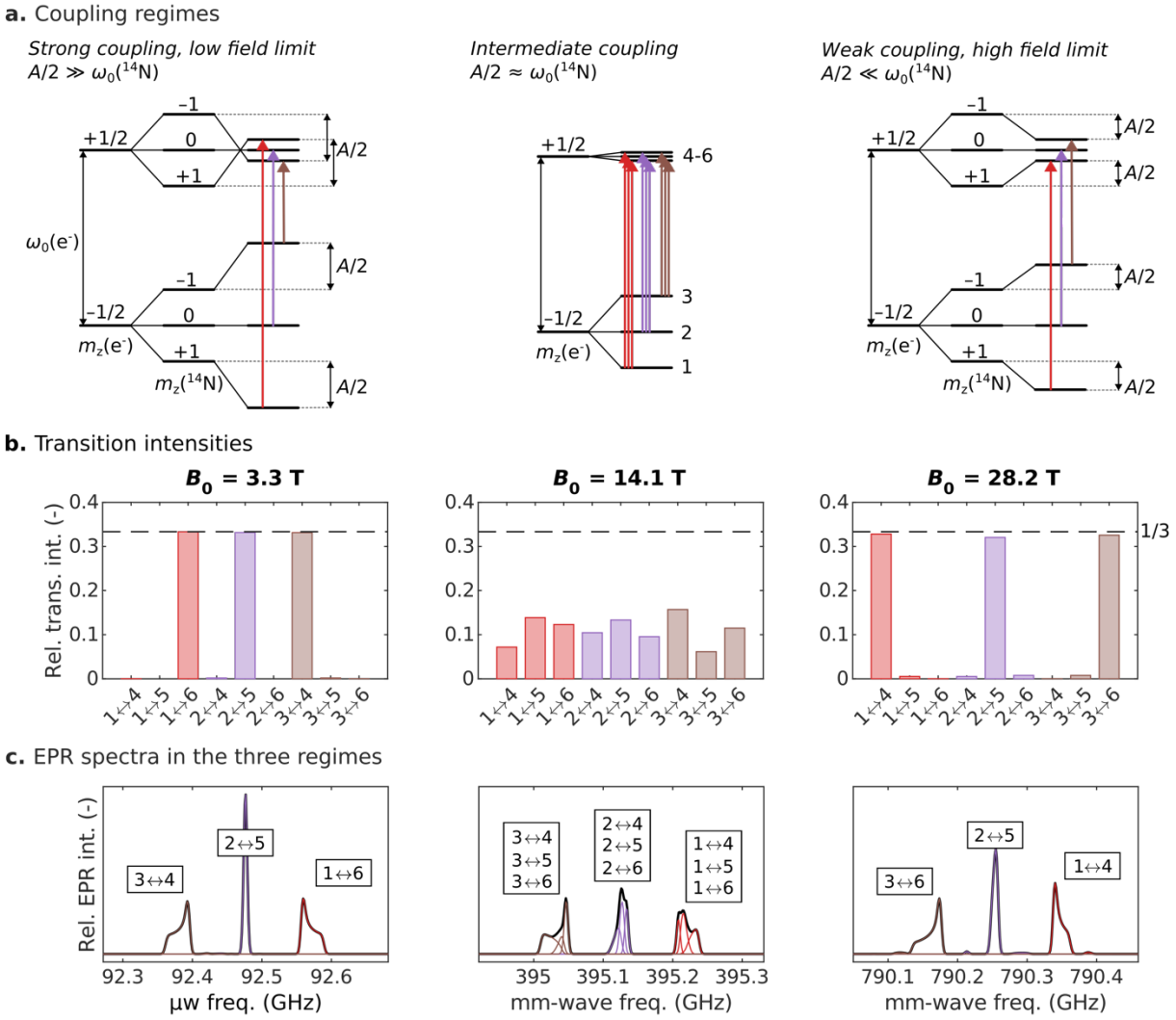

Figure 8: **a**. Energy diagrams of the spin states of the P1 center in different hyperfine coupling regimes. The first, second, and third splittings correspond to the electron Zeeman, ^{14}N Zeeman, and hyperfine interactions, respectively. m_z, $\omega_0(e^-)$, $\omega_0(^{14}N)$, and A are the z projection of the spin angular momentum, the electron and ^{14}N Larmor frequency, and the hyperfine interaction, respectively. Colored arrows show the allowed transitions. **b**. Distribution of the transition intensities in the three regimes. The dashed horizontal lines indicate the maximum intensity of 1/3. **c**. EPR intensities in the three regimes. Colored lines represent the spectra of individual transition between a pair of states

and black lines are the sum of all, i.e., the EPR spectra. Summed spectra are normalized to an integral of 1. Levels are labeled in order of ascending energy (1 = lowest energy, 6 = highest energy).

Conclusion and outlook

In this study, we present MAS DNP profile data of P1 centers of HPHT diamond at 14.1 T and at 35 K, 100 K and RT. This study acquired DNP profiles by frequency, as opposed to field, stepping under MAS, made possible by using mm-wave frequencies from a gyrotron produced by second harmonic generation at half the NMR magnet field and varied by altering the gyrotron cavity temperature at a constant NMR magnetic field. This has practical significance because these measurements could be performed using a regular superconducting NMR magnet without cryogenic field-sweeping capabilities that are typically required for MAS DNP powered by a gyrotron. There are only few studies that feature frequency tuned gyrotrons for DNP,[42,43,45,46] and even fewer that measures MAS-DNP profiles by frequency tuning.[36,42] The temperature of the resonant cavity in our system can be varied from 10 to 65 ºC, yielding a mm-wave frequency range of 260 MHz centered at 395.3 GHz with a stable power (about 1/3 variation on the available range). With this approach, the mm-wave frequency had a standard deviation below 3 MHz, which is sufficiently narrow for stable irradiation even using bi-radicals with narrow matching conditions like trityl-nitroxide.[67] We found that the relation between the cavity temperature and the output frequency could vary over the course of months. We are currently working at equipping our system with real-time monitoring of the mm-wave frequency. This will allow us to correct for small frequency variations during experiments if changes occur. In its current design, our gyrotron outputs only ~1 W compared to up to 50 W, found in state-of-the-art setups.[46,68]

The current gyrotron prototype was designed to provide aggressive frequency tuning of > 1 GHz with a combination of beam voltage, magnetic field and cavity temperature variations. However, the experimentally achieved output power is strongly dependent on the frequency of the beam voltage and magnetic tuning. Hence, primarily temperature tuning was used in these experiments to get stable mm-wave power across the frequency range of the DNP profile. Besides, with the wide tuning band, the resonant frequency of the output window was not optimal resulting in about a reflection of 50 % of the power back into the gyrotron. A new gyrotron is under development with a more modest tuning range with a power of > 5 W across 650 MHz and > 10 W across 150 MHz. In this new gyrotron, we will correct the window thickness and change the operating mode to achieve higher output power. An upgraded gyrotron control system software will allow for the optimization of other operating parameters to achieve constant power of >5 W across the 650 MHz band.

By controlling the gyrotron frequency through the cavity temperature the stability of the mm-wave power is ascertained. Indeed, the power of our gyrotron decreases only by about 1/3 as temperature is increased on the available range, while holding the beam current and other parameters constant. As a comparison, the approach consisting of varying the anode voltage used by Barnes and coworkers allows for a µs time-resolution of the frequency but the resulting power varies by almost an order of magnitude over 340 MHz.[43] The approach of varying the gyrotron magnetic field used by Fujiwara and coworkers also results in power variations up to a factor of 4 over 1 GHz. The testimony to this approach is the high-quality DNP profiles acquired at 35 K to RT that not only recapitulated the previous physical model for P1 centers in HPHT diamond but could significantly improve the model.

Our DNP results furthermore demonstrated the versatility of P1 centers in diamond as highly efficient polarizing agents for ^{13}C-DNP in diamond across a wide range of experimental conditions, from 35 K to RT and both under MAS and in static conditions. A high ^{13}C enhancement of 700 was obtained at RT despite the relatively weak mm-wave power used here (~1 W). By modeling the experimental ^{13}C-DNP profiles, we found that the SE and CE among isolated P1 spins were not significant at the magnetic field used here, i.e., 14.1 T due to the absence of pair of isolated P1 spins fulfilling the CE matching condition.[24,26] The experimental profiles were well reproduced using the CE involving clustered spins and tCE, where ^{13}C nuclear spins are polarized by triple-spin flips involving slow-relaxing isolated or dipolar-coupled P1 spins, fast-relaxing exchange-coupled P1 pairs, and ^{13}C nuclear spins. We introduced a new approach to modeling tCE by combining an analytical solution to spectral diffusion[61] and iCE.[59] These results firmly validate the dominant presence of clusters of P1 spins with significant dipolar and exchange coupling in HPHT diamonds, and showcase their utility for DNP. The results cannot be explained using homogeneously distributed P1 spins, as the DNP efficiency observed at 14 T and RT relies on the presence of clustered P1 spins.

The quantification of the clustering effect of P1 spins is important for the field of quantum sensing using NV centers or hyperpolarized ^{13}C signal given their strong influence on the property of NV centers. Many studies focus on understanding and mitigating the decoherence of NV centers for which P1 centers are known to be a major source of decoherence.[69–72] However, the model of HPHT diamond in the literature until recently did not consider dominant populations of exchange coupled P1 centers. Published models of NV decoherence assume homogeneously distributed P1 spins,[69] and therefore do not account for clustering that will change the influence of P1 on NV spin properties. Indeed, being closer together, P1 spin clusters should undergo faster flip-flops, which would decrease the spectral density of spin state fluctuations at 0 frequency. This should in turn increase the coherence time of NV spins. Furthermore, the presence of exchange-coupled P1 spin pairs is not accounted for in models of NV decoherence.[69,72] Although the significant exchange coupling evidenced previously[31] and confirmed here can be expected to influence NV decoherence, it is not obvious in what direction it should affect it. Incorporating this coupling in NV decoherence models is therefore necessary to better understand, and thus develop strategies for limiting, NV decoherence.

Acknowledgements

The authors wish to thank Joshua Straub for many helpful discussions on the manuscript and Ewoud Vaneeckhaute for discussion on the modeling of spectral diffusion. We also thank the JEOL team, in particular Suematsu San for his continued support for the instrument development. SH and CT acknowledge support for DNP development efforts from the National Institutes of Health (NIH) by grant R01AG056058. This work was funded by the NSF (CHE CMI #2411584) awarded to SH; by the SNSF Postdoc.Mobility scheme awarded to QS; and the ISRAEL SCIENCE FOUNDATION (grant No. 1058/23) awarded to IK.

Declaration of Competing Interest

The authors declare that they have no known competing financial interests or personal relationships that could have appeared to influence the work reported in this paper.

Data and code availability

The data presented in this work, the codes used to analyze them, and the codes used for simulation will be deposited on a repository once the paper is accepted for publication.

Sample and Methods

Gyrotron Frequency and Power Measurements. mm-wave irradiation in our setup for DNP measurements was enabled by a Bridge 12 gyrotron tube assembly, described in more complete detail in the Supplementary Material. The output mm-wave frequency is determined by the dimensions of the internal cavity which supports a second harmonic transverse electric (TE) mode at 395 GHz when subjected to the external magnetic field of a 7.3 T cryogen-free superconducting magnet (Cryogen Inc.). The cavity is thermally isolated from the electron gun and internal converter regions, thus allowing tuning of the mm-wave frequency by adjusting the cavity temperature. Heating or cooling of the cavity causes expansion or contraction of the metal walls respectively, thus changing its overall dimensions and the resulting mm-wave frequency, typically at a rate of ~5 MHz/^{o}C. A Polyscience chiller with a water bath provides temperature tuning for the gyrotron cavity within a range of 10°C to 67.5°C.

To determine the temperature to mm-wave frequency correlation of the gyrotron cavity, the frequency of the mm-wave beam was measured using a frequency measurement system (FMS) by Bridge12. The FMS operates by mixing a local oscillator frequency ν_{LO} and that of the gyrotron mm-wave frequency ν_{mw}, such that

$$\nu_{IF} = \lfloor \nu_{mw} \pm n\nu_{LO} \rfloor, \qquad \text{Eq. 6}$$

where n is the harmonic and ν_{IF} is the intermediate frequency. Because it does not feature a bandpass filter, the FMS displays both the upper and lower side band, and all other possible leaked frequencies of the gyrotron from lower stages, if they exist. The FMS software can automatically detect and classify the sidebands and provides a unique frequency measurement with an accuracy ±1 MHz. The gyrotron frequency was measured by removing a portion of the waveguide and placing a mirror approximately 1 m away from the gyrotron cavity output, reflecting at a 45^{o} angle, and positioning the frequency measurement system (FMS) 25.4 cm away from the mirror.

The power output of the gyrotron was measured using a Scientech power meter, placed approximately 1 m away from the output window along the waveguide. To determine the actual power, the measured value was adjusted by a calibration factor of 2.75. This calibration factor was obtained by a combination of water and dry calorimeter to account for the measured (absorbed) power compared to the real power (including both absorbed and reflected power). The reflection/absorption of the Scientech calorimeter head (ACS5000S) was measured on a Vector Network analyzer to determine the correction factor. While the gyrotron power is constant at approximately 1 W during cavity temperature tuning, it changes significantly during tuning of any other gyrotron parameters including cathode voltage, beam current, and gyrotron magnetic field.

Sample Preparation. All DNP experiments were performed on a sample of ~40-mg of High-pressure high temperature (HPHT) Type Ib diamond manufactured by Element 6. The nitrogen concentration in the diamond and the particle size were estimated by the manufacturer to be 110-130 ppm and 15-25 µm,

respectively. The sample was centered in a 3.2 mm Si_3N_4 rotor sleeve using Kel-F spacers. The rotor was sealed using Vespel caps containing Dyneema fiber reinforced plastic inserts.

NMR Measurements. All ^{13}C NMR measurements were performed on a 14.1 T NMR DNP spectrometer equipped with a closed-cycle helium ULT-MAS system described previously,[47] using a JEOL HX double resonance probe (see SI, Section 1a). ^{13}C NMR spectra were acquired using the Delta v6.0 NMR acquisition and data processing software from JEOL. Saturation recovery measurements were performed with the pulse sequence: (t_{sat})– τ –π/2-detection, where the saturation pulse train uses t_{sat} = $(\pi/2–t_{wait})_n$ = 10 ms, with t_{wait} = 1 ms, τ = 60 s and π/2 = 4.5 µs or 7.0 µs with 15 dB or 24 dB attenuation at RT and ULT, respectively, from the full power for both saturation and detection. For DNP experiments, continuous wave (CW) mm-wave irradiation was applied throughout the pulse sequence, and the data was acquired with two scans at each mm-wave frequency. For T_1 and T_{DNP} build-up curve measurements, the same saturation-recovery pulse sequence was used without and with mm-wave irradiation respectively, and by varying the time interval τ from 0.1 s to 6 h. The spectra were exported as raw FID data from the Delta software and processed using the Python DNPLab package v2.1.19.

EPR Measurements. EPR experiments were performed on a home-built 13.8 T dual DNP/EPR spectrometer equipped with a closed-cycle helium cooling system and using a home-built pulse forming unit, an amplifier multiplier chain (AMC), and a quasi-optical induction mode bridge, as described elsewhere.[66,66] Frequency-swept EPR signals were measured using an echo sequence $(t_p)_{\phi1} – \tau_e – (t_p)_{\phi2} – \tau_e – (\text{detection})_{\phi d}$ with a 16-step phase cycling ϕ_1 = [0°$_4$, 90°$_4$, 180°$_4$, 270°$_4$] and ϕ_2 = [0°, 90°, 180°, 270°]$_4$ for the two pulses and $\phi_d = \phi_1 - 2\phi_2$ for detection. At RT, the pulse length and echo time were t_p = 1.6 µs and τ_e = 0.5 µs, respectively, and the signal was averaged over 100 shots with a repetition time of 2 ms. At 35 K, the pulse length and echo time were t_p = 1.8 µs and τ_e = 0.85 µs, respectively and the signal was recorded with a single shot and a repetition time of 1 s. Saturation experiments were performed by adding a pump pulse of length t_{pump} = 10 ms at the same frequency as the probe, with a delay τ_d of 1 µs between the pump and probe blocks. The pulse length and echo time τ_e for each temperature were the same as in the frequency-swept EPR experiments with 50 averages at RT and a single shot at 35 K and a repetition time of 14 ms and 0.5 s for the RT and 35 K experiments respectively.

The spin counting was performed on a CW X-band Bruker Elexsys E500 spectrometer.

Data Processing. The DNP profiles were processed using python scripts primarily using the DNPLab python package developed in collaboration with Bridge12. The DNP profiles are shown using the on/off signal enhancement at time τ after saturation

$$\epsilon_{\text{on/off}}(\tau) = \frac{I_{\text{on}}(\tau)}{I_{\text{off}}(\tau)}, \qquad \text{Eq. 7}$$

where $I_{on}(\tau)$ and $I_{off}(\tau)$ are the signal integrals at time τ after saturation with and without µw irradiation respectively. The absolute enhancement is defined as

$$\epsilon(\tau) = \frac{I_{\text{on}}(\tau)}{I_{\text{off}}(\infty)}, \qquad \text{Eq. 8}$$

where the mm-wave-off integral is taken at $\tau \rightarrow \infty$, i.e., after full relaxation.

EPR and DNP Simulations. EPR spectra of P1 centers were simulated with the MATLAB package EasySpin, using the *pepper* function (for powder-averaged spectra). EPR parameters for the P1 centers are based on

recently reported values from Ref [31]: g-factors $g_{\parallel}$ = 2.00218 and $g_{\perp}$ = 2.00220); P1-^{14}N hyperfine interaction values $A_{\parallel}/2\pi$ = 114.0 MHz and $A_{\perp}/2\pi$ = 81.3 MHz; ^{14}N quadrupolar constant $P_{\parallel}/2\pi$ = -3.97 MHz ; Gaussian line broadening of 5 MHz for isolated P1 centers, and of 30 and 17.5 MHz for dipolar-broadened clusters and exchange-coupled P1 pairs, respectively; an exchange coupling of $J/2\pi$ = 138.7 MHz for the exchange-coupled P1 pairs. The relative contributions of the isolated, dipolar-broadened and exchange-coupled P1 spins to the overall EPR line are 0.49, 0.38, and 0.13, respectively. In addition to the values reported in Ref. [31], a dipolar coupling of 50 MHz was assumed between the exchange-coupled P1 pairs (see the text for more detail). The obtained EPR line was used for all simulations in the paper using home-written MATLAB scripts. See the Supplement for details on the simulation method.

References

(1) Corzilius, B. High-Field Dynamic Nuclear Polarization. *Annu. Rev. Phys. Chem.* **2020**, *71* (Volume 71, 2020), 143–170. https://doi.org/10.1146/annurev-physchem-071119-040222.

(2) Bertarello, A.; Berruyer, P.; Artelsmair, M.; Elmore, C. S.; Heydarkhan-Hagvall, S.; Schade, M.; Chiarparin, E.; Schantz, S.; Emsley, L. In-Cell Quantification of Drugs by Magic-Angle Spinning Dynamic Nuclear Polarization NMR. *J. Am. Chem. Soc.* **2022**, *144* (15), 6734–6741. https://doi.org/10.1021/jacs.1c12442.

(3) *Quantitative dynamic nuclear polarization-NMR on blood plasma for assays of drug metabolism - Lerche - 2011 - NMR in Biomedicine - Wiley Online Library*. https://analyticalsciencejournals.onlinelibrary.wiley.com/doi/abs/10.1002/nbm.1561 (accessed 2024-06-13).

(4) Nelson, S. J.; Kurhanewicz, J.; Vigneron, D. B.; Larson, P. E. Z.; Harzstark, A. L.; Ferrone, M.; van Criekinge, M.; Chang, J. W.; Bok, R.; Park, I.; Reed, G.; Carvajal, L.; Small, E. J.; Munster, P.; Weinberg, V. K.; Ardenkjaer-Larsen, J. H.; Chen, A. P.; Hurd, R. E.; Odegardstuen, L.-I.; Robb, F. J.; Tropp, J.; Murray, J. A. Metabolic Imaging of Patients with Prostate Cancer Using Hyperpolarized [1-^{13} C]Pyruvate. *Sci. Transl. Med.* **2013**, *5* (198). https://doi.org/10.1126/scitranslmed.3006070.

(5) Sahin, O.; De Leon Sanchez, E.; Conti, S.; Akkiraju, A.; Reshetikhin, P.; Druga, E.; Aggarwal, A.; Gilbert, B.; Bhave, S.; Ajoy, A. High Field Magnetometry with Hyperpolarized Nuclear Spins. *Nat. Commun.* **2022**, *13* (1), 5486. https://doi.org/10.1038/s41467-022-32907-8.

(6) Shim, J. H.; Niemeyer, I.; Zhang, J.; Suter, D. Room-Temperature High-Speed Nuclear-Spin Quantum Memory in Diamond. *Phys. Rev. A* **2013**, *87* (1), 012301. https://doi.org/10.1103/PhysRevA.87.012301.

(7) Bucher, D. B. Principles of Nano- and Microscale NMR-Spectroscopy with NV-Diamond Sensors. **2019**, *8*.

(8) Wickenbrock, A.; Zheng, H.; Bougas, L.; Leefer, N.; Afach, S.; Jarmola, A.; Acosta, V. M.; Budker, D. Microwave-Free Magnetometry with Nitrogen-Vacancy Centers in Diamond. *Appl. Phys. Lett.* **2016**, *109* (5), 053505. https://doi.org/10.1063/1.4960171.

(9) Loretz, M.; Rosskopf, T.; Degen, C. L. Radio-Frequency Magnetometry Using a Single Electron Spin. *Phys. Rev. Lett.* **2013**, *110* (1), 017602. https://doi.org/10.1103/PhysRevLett.110.017602.

(10) Balasubramanian, G.; Chan, I. Y.; Kolesov, R.; Al-Hmoud, M.; Tisler, J.; Shin, C.; Kim, C.; Wojcik, A.; Hemmer, P. R.; Krueger, A.; Hanke, T.; Leitenstorfer, A.; Bratschitsch, R.; Jelezko, F.; Wrachtrup, J. Nanoscale Imaging Magnetometry with Diamond Spins under Ambient Conditions. *Nature* **2008**, *455* (7213), 648–651. https://doi.org/10.1038/nature07278.

(11) Waddington, D. E. J.; Boele, T.; Rej, E.; McCamey, D. R.; King, N. J. C.; Gaebel, T.; Reilly, D. J. Phase-Encoded Hyperpolarized Nanodiamond for Magnetic Resonance Imaging. *Sci. Rep.* **2019**, *9* (1), 5950. https://doi.org/10.1038/s41598-019-42373-w.
(12) Lilly Thankamony, A. S.; Wittmann, J. J.; Kaushik, M.; Corzilius, B. Dynamic Nuclear Polarization for Sensitivity Enhancement in Modern Solid-State NMR. *Prog. Nucl. Magn. Reson. Spectrosc.* **2017**, *102–103*, 120–195. https://doi.org/10.1016/j.pnmrs.2017.06.002.
(13) J. Kubicki, D.; Casano, G.; Schwarzwälder, M.; Abel, S.; Sauvée, C.; Ganesan, K.; Yulikov, M.; J. Rossini, A.; Jeschke, G.; Copéret, C.; Lesage, A.; Tordo, P.; Ouari, O.; Emsley, L. Rational Design of Dinitroxide Biradicals for Efficient Cross-Effect Dynamic Nuclear Polarization. *Chem. Sci.* **2016**, *7* (1), 550–558. https://doi.org/10.1039/C5SC02921J.
(14) Equbal, A.; Li, Y.; Leavesley, A.; Huang, S.; Rajca, S.; Rajca, A.; Han, S. Truncated Cross Effect Dynamic Nuclear Polarization: An Overhauser Effect Doppelgänger. *J. Phys. Chem. Lett.* **2018**, *9* (9), 2175–2180. https://doi.org/10.1021/acs.jpclett.8b00751.
(15) Plainchont, B.; Berruyer, P.; Dumez, J.-N.; Jannin, S.; Giraudeau, P. Dynamic Nuclear Polarization Opens New Perspectives for NMR Spectroscopy in Analytical Chemistry. *Anal. Chem.* **2018**, *90* (6), 3639–3650. https://doi.org/10.1021/acs.analchem.7b05236.
(16) Rankin, A. G.; Trébosc, J.; Pourpoint, F.; Amoureux, J.-P.; Lafon, O. Recent Developments in MAS DNP-NMR of Materials. *Solid State Nucl. Magn. Reson.* **2019**, *101*, 116–143.
(17) Ardenkjaer-Larsen, J. H. Hyperpolarized MR – What's up Doc? *J. Magn. Reson.* **2019**, *306*, 124–127. https://doi.org/10.1016/j.jmr.2019.07.017.
(18) Berruyer, P.; Björgvinsdóttir, S.; Bertarello, A.; Stevanato, G.; Rao, Y.; Karthikeyan, G.; Casano, G.; Ouari, O.; Lelli, M.; Reiter, C.; Engelke, F.; Emsley, L. Dynamic Nuclear Polarization Enhancement of 200 at 21.15 T Enabled by 65 kHz Magic Angle Spinning. *J. Phys. Chem. Lett.* **2020**, *11* (19), 8386–8391. https://doi.org/10.1021/acs.jpclett.0c02493.
(19) Kaushik, M.; Lingua, H.; Stevanato, G.; Elokova, M.; Lelli, M.; Lesage, A.; Ouari, O. Trehalose Matrices for High Temperature Dynamic Nuclear Polarization Enhanced Solid State NMR. *Phys. Chem. Chem. Phys.* **2022**, *24* (20), 12167–12175. https://doi.org/10.1039/D2CP00970F.
(20) Wu, Y.; Weil, T. Recent Developments of Nanodiamond Quantum Sensors for Biological Applications. *Adv. Sci.* **2022**, *9* (19), 2200059. https://doi.org/10.1002/advs.202200059.
(21) Segawa, T. F.; Igarashi, R. Nanoscale Quantum Sensing with Nitrogen-Vacancy Centers in Nanodiamonds – A Magnetic Resonance Perspective. *Prog. Nucl. Magn. Reson. Spectrosc.* **2023**, *134–135*, 20–38. https://doi.org/10.1016/j.pnmrs.2022.12.001.
(22) Balmer, R. S.; Brandon, J. R.; Clewes, S. L.; Dhillon, H. K.; Dodson, J. M.; Friel, I.; Inglis, P. N.; Madgwick, T. D.; Markham, M. L.; Mollart, T. P.; Perkins, N.; Scarsbrook, G. A.; Twitchen, D. J.; Whitehead, A. J.; Wilman, J. J.; Woollard, S. M. Chemical Vapour Deposition Synthetic Diamond: Materials, Technology and Applications. *J. Phys. Condens. Matter* **2009**, *21* (36), 364221. https://doi.org/10.1088/0953-8984/21/36/364221.
(23) Reina, G.; Zhao, L.; Bianco, A.; Komatsu, N. Chemical Functionalization of Nanodiamonds: Opportunities and Challenges Ahead. *Angew. Chem. Int. Ed.* **2019**, *58* (50), 17918–17929. https://doi.org/10.1002/anie.201905997.
(24) Casabianca, L. B.; Shames, A. I.; Panich, A. M.; Shenderova, O.; Frydman, L. Factors Affecting DNP NMR in Polycrystalline Diamond Samples. *J. Phys. Chem. C* **2011**, *115* (39), 19041–19048. https://doi.org/10.1021/jp206167j.
(25) Fischer, R.; Bretschneider, C. O.; London, P.; Budker, D.; Gershoni, D.; Frydman, L. Bulk Nuclear Polarization Enhanced at Room Temperature by Optical Pumping. *Phys. Rev. Lett.* **2013**, *111* (5), 057601. https://doi.org/10.1103/PhysRevLett.111.057601.
(26) Bretschneider, C. O.; Akbey, Ü.; Aussenac, F.; Olsen, G. L.; Feintuch, A.; Oschkinat, H.; Frydman, L. On The Potential of Dynamic Nuclear Polarization Enhanced Diamonds in Solid-State and

Dissolution ^{13}C NMR Spectroscopy. *ChemPhysChem* **2016**, *17* (17), 2691–2701. https://doi.org/10.1002/cphc.201600301.
(27) Nevzorov, A. A.; Marek, A.; Milikisiyants, S.; Smirnov, A. I. Characterization of Photonic Band Resonators for DNP NMR of Thin Film Samples at 7 T Magnetic Field. *J. Magn. Reson.* **2021**, *323*, 106893. https://doi.org/10.1016/j.jmr.2020.106893.
(28) Shimon, D.; Cantwell, K. A.; Joseph, L.; Williams, E. Q.; Peng, Z.; Takahashi, S.; Ramanathan, C. Large Room Temperature Bulk DNP of ^{13}C via P1 Centers in Diamond. *J. Phys. Chem. C* **2022**, *126* (41), 17777–17787. https://doi.org/10.1021/acs.jpcc.2c06145.
(29) Shimon, D.; Cantwell, K.; Joseph, L.; Ramanathan, C. Room Temperature DNP of Diamond Powder Using Frequency Modulation. *Solid State Nucl. Magn. Reson.* **2022**, *122*, 101833. https://doi.org/10.1016/j.ssnmr.2022.101833.
(30) Bussandri, S.; Shimon, D.; Equbal, A.; Ren, Y.; Takahashi, S.; Ramanathan, C.; Han, S. P1 Center Electron Spin Clusters Are Prevalent in Type Ib Diamonds. *J. Am. Chem. Soc.* **2023**, jacs.3c06705. https://doi.org/10.1021/jacs.3c06705.
(31) Nir-Arad, O.; Shlomi, D. H.; Manukovsky, N.; Laster, E.; Kaminker, I. Nitrogen Substitutions Aggregation and Clustering in Diamonds as Revealed by High-Field Electron Paramagnetic Resonance. *J. Am. Chem. Soc.* **2023**, jacs.3c06739. https://doi.org/10.1021/jacs.3c06739.
(32) Nevzorov, A. A.; Marek, A.; Milikisiyants, S.; Smirnov, A. I. High-Frequency High-Power DNP/EPR Spectrometer Operating at 7 T Magnetic Field. *J. Magn. Reson.* **2024**, *362*, 107677. https://doi.org/10.1016/j.jmr.2024.107677.
(33) Witte, G. von; Himmler, A.; Tamarov, K.; Moilanen, J. O.; Ernst, M.; Kozerke, S. Temperature-Dependent Dynamic Nuclear Polarization of Diamond. arXiv December 17, 2024. https://doi.org/10.48550/arXiv.2412.12663.
(34) Childress, L.; Hanson, R. Diamond NV Centers for Quantum Computing and Quantum Networks. *MRS Bull.* **2013**, *38* (2), 134–138. https://doi.org/10.1557/mrs.2013.20.
(35) Palani, R. S.; Mardini, M.; Quan, Y.; Ouyang, Y.; Mishra, A.; Griffin, R. G. Dynamic Nuclear Polarization with P1 Centers in Diamond. *J. Phys. Chem. Lett.* **2024**, 11504–11509. https://doi.org/10.1021/acs.jpclett.4c02612.
(36) Kato, K.; Takahashi, H.; Tamaki, H.; Fujiwara, T.; Matsuki, Y. *Nanodiamond-Based Hyperpolarization for in-Situ Magic-Angle-Spinning Nuclear Magnetic Resonance Spectroscopy of Proteins*; preprint; Chemistry, 2023. https://doi.org/10.26434/chemrxiv-2023-x9m17-v2.
(37) Panich, A. M.; Sergeev, N. A.; Goren, S. D. Location of Paramagnetic Defects in Detonation Nanodiamond from Proton Spin-Lattice Relaxation Data. *Solid State Nucl. Magn. Reson.* **2020**, *105*, 101624. https://doi.org/10.1016/j.ssnmr.2019.101624.
(38) Panich, A. M.; Aleksenskii, A. E.; Yudina, E. B.; Vul', A. Ya. Spatially Resolved Spin–Lattice Relaxation Times and Line Widths in Manganese-Grafted Detonation Nanodiamonds. *J. Phys. Chem. C* **2022**, *126* (3), 1489–1495. https://doi.org/10.1021/acs.jpcc.1c09026.
(39) Shames, A. I.; Osipov, V. Yu.; Bogdanov, K. V.; Baranov, A. V.; Zhukovskaya, M. V.; Dalis, A.; Vagarali, S. S.; Rampersaud, A. Does Progressive Nitrogen Doping Intensify Negatively Charged Nitrogen Vacancy Emission from E-Beam-Irradiated Ib Type High-Pressure–High-Temperature Diamonds? *J. Phys. Chem. C* **2017**, *121* (9), 5232–5240. https://doi.org/10.1021/acs.jpcc.6b12827.
(40) Nir-Arad, O.; Laster, E.; Daksi, M.; Manukovsky, N.; Kaminker, I. On the Peculiar EPR Spectra of P1 Centers at High (12–20 T) Magnetic Fields. *Phys. Chem. Chem. Phys.* **2024**, *26* (43), 27633–27647. https://doi.org/10.1039/D4CP03055A.
(41) Idehara, T.; Kosuga, K.; Agusu, L.; Ikeda, R.; Ogawa, I.; Saito, T.; Matsuki, Y.; Ueda, K.; Fujiwara, T. Continuously Frequency Tunable High Power Sub-THz Radiation Source—Gyrotron FU CW VI for 600 MHz DNP-NMR Spectroscopy. *J. Infrared Millim. Terahertz Waves* **2010**, *31* (7), 775–790. https://doi.org/10.1007/s10762-010-9643-y.

(42) Matsuki, Y.; Ueda, K.; Idehara, T.; Ikeda, R.; Ogawa, I.; Nakamura, S.; Toda, M.; Anai, T.; Fujiwara, T. Helium-Cooling and -Spinning Dynamic Nuclear Polarization for Sensitivity-Enhanced Solid-State NMR at 14T and 30K. *J. Magn. Reson.* **2012**, *225*, 1–9. https://doi.org/10.1016/j.jmr.2012.09.008.
(43) Gao, C.; Alaniva, N.; Saliba, E. P.; Sesti, E. L.; Judge, P. T.; Scott, F. J.; Halbritter, T.; Sigurdsson, S. Th.; Barnes, A. B. Frequency-Chirped Dynamic Nuclear Polarization with Magic Angle Spinning Using a Frequency-Agile Gyrotron. *J. Magn. Reson.* **2019**, *308*, 106586. https://doi.org/10.1016/j.jmr.2019.106586.
(44) Millen, M.; Pagonakis, I. Gr.; Björgvinsdóttir, S.; Alaniva, N.; Barnes, A. B. Control and Manipulation of Microwave Polarization and Power of a Frequency-Agile 198 GHz Gyrotron for Magnetic Resonance. *J. Infrared Millim. Terahertz Waves* **2023**, *44* (3–4), 281–296. https://doi.org/10.1007/s10762-023-00907-4.
(45) Denysenkov, V.; Prandolini, M. J.; Gafurov, M.; Sezer, D.; Endeward, B.; Prisner, T. F. Liquid State DNP Using a 260 GHz High Power Gyrotron. *Phys. Chem. Chem. Phys.* **2010**, *12* (22), 5786. https://doi.org/10.1039/c003697h.
(46) Levien, M.; Yang, L.; Van Der Ham, A.; Reinhard, M.; John, M.; Purea, A.; Ganz, J.; Marquardsen, T.; Tkach, I.; Orlando, T.; Bennati, M. Overhauser Enhanced Liquid State Nuclear Magnetic Resonance Spectroscopy in One and Two Dimensions. *Nat. Commun.* **2024**, *15* (1), 5904. https://doi.org/10.1038/s41467-024-50265-5.
(47) Li, Y.; Chaklashiya, R.; Takahashi, H.; Kawahara, Y.; Tagami, K.; Tobar, C.; Han, S. Solid-State MAS NMR at Ultra Low Temperature of Hydrated Alanine Doped with DNP Radicals. *J. Magn. Reson.* **2021**, *333*, 107090. https://doi.org/10.1016/j.jmr.2021.107090.
(48) Mentink-Vigier, F.; Barra, A.-L.; Van Tol, J.; Hediger, S.; Lee, D.; De Paëpe, G. *De Novo* Prediction of Cross-Effect Efficiency for Magic Angle Spinning Dynamic Nuclear Polarization. *Phys. Chem. Chem. Phys.* **2019**, *21* (4), 2166–2176. https://doi.org/10.1039/C8CP06819D.
(49) Cox, A.; Newton, M. E.; Baker, J. M. ^{13} C, ^{14} N and ^{15} N ENDOR Measurements on the Single Substitutional Nitrogen Centre (P1) in Diamond. *J. Phys. Condens. Matter* **1994**, *6* (2), 551–563. https://doi.org/10.1088/0953-8984/6/2/025.
(50) Overhauser, A. W. Polarization of Nuclei in Metals. *Phys. Rev.* **1953**, *92* (2), 411–415. https://doi.org/10.1103/PhysRev.92.411.
(51) Järvinen, J.; Zvezdov, D.; Ahokas, J.; Sheludiakov, S.; Lehtonen, L.; Vasiliev, S.; Vlasenko, L.; Ishikawa, Y.; Fujii, Y. Dynamic Nuclear Polarization and ESR Hole Burning in As Doped Silicon. *Phys. Chem. Chem. Phys.* **2020**, *22* (18), 10227–10237. https://doi.org/10.1039/C9CP06859G.
(52) Can, T. V.; Caporini, M. A.; Mentink-Vigier, F.; Corzilius, B.; Walish, J. J.; Rosay, M.; Maas, W. E.; Baldus, M.; Vega, S.; Swager, T. M.; Griffin, R. G. Overhauser Effects in Insulating Solids. *J. Chem. Phys.* **2014**, *141* (6), 064202. https://doi.org/10.1063/1.4891866.
(53) Ji, X.; Can, T. V.; Mentink-Vigier, F.; Bornet, A.; Milani, J.; Vuichoud, B.; Caporini, M. A.; Griffin, R. G.; Jannin, S.; Goldman, M.; Bodenhausen, G. Overhauser Effects in Non-Conducting Solids at 1.2 K. *J. Magn. Reson.* **2018**, *286*, 138–142. https://doi.org/10.1016/j.jmr.2017.11.017.
(54) Gurinov, A.; Sieland, B.; Kuzhelev, A.; Elgabarty, H.; Kühne, T. D.; Prisner, T.; Paradies, J.; Ivanov, K. L.; Pylaeva, S. Mixed-Valence Compounds as Polarizing Agents for Overhauser Dynamic Nuclear Polarization in Solids. *Angew Chem Int Ed* **2021**, *60* (28), 15371–15375. https://doi.org/doi.org/10.1002/anie.202103215.
(55) Abragam, A.; Goldman, M. Principles of Dynamic Nuclear Polarisation. *Rep. Prog. Phys.* **1978**, *41* (3), 395–467. https://doi.org/10.1088/0034-4885/41/3/002.
(56) Thurber, K. R.; Tycko, R. Theory for Cross Effect Dynamic Nuclear Polarization under Magic-Angle Spinning in Solid State Nuclear Magnetic Resonance: The Importance of Level Crossings. *J. Chem. Phys.* **2012**, *137* (8), 084508. https://doi.org/10.1063/1.4747449.

(57) Mentink-Vigier, F.; Akbey, Ü.; Hovav, Y.; Vega, S.; Oschkinat, H.; Feintuch, A. Fast Passage Dynamic Nuclear Polarization on Rotating Solids. *J. Magn. Reson.* **2012**, *224*, 13–21. https://doi.org/10.1016/j.jmr.2012.08.013.
(58) Banerjee, D.; Shimon, D.; Feintuch, A.; Vega, S.; Goldfarb, D. The Interplay between the Solid Effect and the Cross Effect Mechanisms in Solid State 13C DNP at 95 GHz Using Trityl Radicals. *J. Magn. Reson.* **2013**, *230*, 212–219. https://doi.org/10.1016/j.jmr.2013.02.010.
(59) Kundu, K.; Feintuch, A.; Vega, S. Theoretical Aspects of the Cross Effect Enhancement of Nuclear Polarization under Static Dynamic Nuclear Polarization Conditions. *J. Phys. Chem. Lett.* **2019**, *10* (8), 1769–1778. https://doi.org/10.1021/acs.jpclett.8b03615.
(60) Vaneeckhaute, E.; Bocquelet, C.; Rougier, N.; Jegadeesan, S. A.; Vinod-Kumar, S.; Mathies, G.; Melzi, R.; Kempf, J.; Stern, Q.; Jannin, S. Dynamic Nuclear Polarization Mechanisms Using TEMPOL and Trityl OX063 Radicals at 1 T and 77 K. 2024. https://doi.org/10.48550/arXiv.2412.10325.
(61) Wenckebach, W. Th. Spectral Diffusion of Electron Spin Polarization in Glasses Doped with Radicals for DNP. *J. Magn. Reson.* **2024**, *360*, 107651. https://doi.org/10.1016/j.jmr.2024.107651.
(62) Hovav, Y.; Kaminker, I.; Shimon, D.; Feintuch, A.; Goldfarb, D.; Vega, S. The Electron Depolarization during Dynamic Nuclear Polarization: Measurements and Simulations. *Phys. Chem. Chem. Phys.* **2015**, *17* (1), 226–244. https://doi.org/10.1039/C4CP03825H.
(63) Kundu, K.; Cohen, M. R.; Feintuch, A.; Goldfarb, D.; Vega, S. Experimental Quantification of Electron Spectral-Diffusion under Static DNP Conditions. *Phys. Chem. Chem. Phys.* **2019**, *21* (1), 478–489. https://doi.org/10.1039/C8CP05930F.
(64) Kundu, K.; Mentink-Vigier, F.; Feintuch, A.; Vega, S. DNP Mechanisms. *Handb. High Field Dyn. Nucl. Polariz.* **2019**, 15.
(65) Nir-Arad, O.; Shlomi, D. H.; Israelstam, A.; Amit, T.; Manukovsky, N.; Fialkov, A. B.; Kaminker, I. The CW-EPR Capabilities of a Dual DNP/EPR Spectrometer Operating at 14 and 7 T. *J. Magn. Reson.* **2024**, *360*, 107635. https://doi.org/10.1016/j.jmr.2024.107635.
(66) Nir-Arad, O.; Fialkov, A. B.; Shlomi, D. H.; Manukovsky, N.; Mentink-Vigier, F.; Kaminker, I. High-Field Pulsed EPR Spectroscopy under Magic Angle Spinning. *Sci. Adv.* **2024**, *10* (35), eadq6073. https://doi.org/10.1126/sciadv.adq6073.
(67) Mentink-Vigier, F.; Mathies, G.; Liu, Y.; Barra, A.-L.; Caporini, M. A.; Lee, D.; Hediger, S.; G. Griffin, R.; De Paëpe, G. Efficient Cross-Effect Dynamic Nuclear Polarization without Depolarization in High-Resolution MAS NMR. *Chem. Sci.* **2017**, *8* (12), 8150–8163. https://doi.org/10.1039/C7SC02199B.
(68) Rosay, M.; Blank, M.; Engelke, F. Instrumentation for Solid-State Dynamic Nuclear Polarization with Magic Angle Spinning NMR. *J. Magn. Reson.* **2016**, *264*, 88–98.
(69) Park, H.; Lee, J.; Han, S.; Oh, S.; Seo, H. Decoherence of Nitrogen-Vacancy Spin Ensembles in a Nitrogen Electron-Nuclear Spin Bath in Diamond. *Npj Quantum Inf.* **2022**, *8* (1), 95. https://doi.org/10.1038/s41534-022-00605-4.
(70) Luan, L.; Grinolds, M. S.; Hong, S.; Maletinsky, P.; Walsworth, R. L.; Yacoby, A. Decoherence Imaging of Spin Ensembles Using a Scanning Single-Electron Spin in Diamond. *Sci. Rep.* **2015**, *5* (1), 8119. https://doi.org/10.1038/srep08119.
(71) Bauch, E.; Singh, S.; Lee, J.; Hart, C. A.; Schloss, J. M.; Turner, M. J.; Barry, J. F.; Pham, L. M.; Bar-Gill, N.; Yelin, S. F.; Walsworth, R. L. Decoherence of Ensembles of Nitrogen-Vacancy Centers in Diamond. *Phys. Rev. B* **2020**, *102* (13), 134210. https://doi.org/10.1103/PhysRevB.102.134210.
(72) Stepanov, V.; Takahashi, S. Determination of Nitrogen Spin Concentration in Diamond Using Double Electron-Electron Resonance. *Phys. Rev. B* **2016**, *94* (2), 024421. https://doi.org/10.1103/PhysRevB.94.024421.
(73) Kundu, K.; Feintuch, A.; Vega, S. Electron–Electron Cross-Relaxation and Spectral Diffusion during Dynamic Nuclear Polarization Experiments on Solids. *J. Phys. Chem. Lett.* **2018**, *9* (7), 1793–1802. https://doi.org/10.1021/acs.jpclett.8b00090.

(74) Wenckebach, W. T. Dynamic Nuclear Polarization via the Cross Effect and Thermal Mixing: A. The Role of Triple Spin Flips. *J. Magn. Reson.* **2019**, *299*, 124–134.

Supporting information for

P1 center network in high-pressure high-temperature diamonds is a readily accessible source of nuclear hyperpolarization at 14 T

Quentin Stern,[1] Jinlei Cui,[1] Raj Chaklashiya,[1,2] Celeste Tobar,[1,3] Martyna Judd,[1,4] Orit Nir-Arad,[5] Daphna Shimon,[6] Ilia Kaminker,[5] Hiroki Takahashi,[7] Jagadishwar R. Sirigiri,[8] & Songi Han[1,2†]

[1] Department of Chemistry, Northwestern University, 633 Clark Street, Evanston, 60208, IL, USA.
[2] Materials Department, University of California, Santa Barbara, 93106, CA, USA
[3] Department of Chemistry and Biochemistry, University of California, Santa Barbara, 93106, CA, USA.
[4] Research School of Chemistry, The Australian National University Canberra, ACT 2605, Australia.
[5] School of Chemistry, Tel-Aviv University, 6997801 Tel-Aviv, Israel.
[6] Institute of Chemistry, Hebrew University of Jerusalem, Jerusalem 9190401, Israel.
[7] JEOL Ltd., Akishima, Tokyo, 196-8558, Japan.
[8] Bridge12 Technologies, Inc., Natick, MA, USA.

[†] Correspondence: songi.han@northwestern.edu

Contents

1. Instrumentation

a. Ultra-low temperature MAS-NMR

We used a ULT MAS-NMR setup operating from room temperature down to 35 K using helium gas. This setup, particularly the temperature control, was described in detail in Ref. [47]. In brief, it consists of a 14.1 T wide-bore superconducting magnet, a ULT MAS probe with a helium gas recirculation system for helium-gas cooling and spinning of the sample down to temperatures of 30 K, and a gyrotron using second harmonic generation to produce mm-wave entering the ULT MAS probe from the top via a waveguide. The HX double resonance probe used is similar in nature to the HC double resonance probe used in Ref. [47], except it has additional replaceable capacitors to switch nuclei for X channel tuning. When no additional capacitors are used on the X channel, the frequency is tuned to ^{13}C, which is the configuration that was used in this work. The system is equipped with a top-loading system for sample exchange that was not present in Ref. [47].

b. Gyrotron System

The gyrotron system used here was designed and assembled by Bridge12. It comprises several key components, including a magnetron-injection gun, an internal cavity, an internal mode converter, an output window, and a collector. Prior to the operation, the gyrotron tube underwent high-temperature maintenance over several days to reduce gas pressure and enhance operational stability.

The magnetron-injection gun (MIG) is designed to generate an electron beam at a nominal cathode voltage ranging from 21 to 23 kV, with a beam current of up to 160 mA. The output electron beam is directed into the internal cavity, which as described in the main text, is configured to support second harmonic generation (SHG) in the transverse electric (TE) mode at 395 GHz at a magnetic field of 7.3 T provided by a Cryomagnetic Inc. cryogen-free superconducting magnet. The internal cavity is thermally isolated from the cavity containing the MIG and internal mode converter, allowing frequency tuning via temperature modulation at approximately 5 MHz/°C, with a Polyscience chiller used to adjust the gyrotron cavity temperature between 10 °C and 70 °C.

The internal mode converter transforms the TE mode produced in the cavity into a Gaussian beam which then exits the gyrotron tube through an output window perpendicular to the tube. The output window consists of a single disk of Al_2O_3. The collector, located at the top of the gyrotron tube, dissipates the spent electron beam and is cooled by an SMC thermos water-cooled chiller, set to 15°C, to maintain stability and prevent overheating during operation. Vacuum maintenance of gyrotron tube is facilitated by an VacIon pump from Duniway Stockroom Corp.

The 7.3T cryogen-free magnet, custom-designed and built by Cryomagnetic Inc., utilizes twisted multiple filamentary NbTi wire and operates at 4.2 K. Cooling of the cryogen-free magnet which is achieved through the combined use of a Sumitomo F-70 water-cooled compressor and an RDK-408D2 Sumitomo cold head. The magnet is energized using a Cryomagnetic Model 4G-100 Superconducting Magnet Power Supply, and its temperature is monitored by a Cryomagnetic TM-612 cryogenic temperature monitor with four measurement channels. The configuration of the cryogen-free magnet allows for a reduced path length from the internal cavity to the output window, enhancing system efficiency. The cavity region is positioned inside the 7.3 T magnet, while the electron gun is located within a separate, independently adjustable gun coil, allowing for optimization during gyrotron testing.

The control system, designed to monitor and control various parameters for the operation of the 395 GHz gyrotron, interfaces a Python-based software developed by Bridge12. The software controls operating parameters, including the electron beam voltage and current, body current, gun coil voltage and current, chiller temperatures, and vacuum levels within the gyrotron tube. The interface features a proportional-integral-derivative (PID) controller, which stabilizes the electron beam current by adjusting the filament current. The control system is powered by a modified 4 kW Spellman X-ray power supply (DF series), which provides the necessary high voltage for system operation. Additionally, the two thermos chiller units—one dedicated to the cavity and the other to the collector—can be controlled remotely, allowing for precise management of the system's thermal environment.

The activation of the gyrotron tube follows a specific sequence, beginning with the initiation of the filament current, followed by the gun coil current, and finally the cathode voltage. The output power and frequency of the mm-wave radiation depend on several factors, including the cathode voltage, beam current, cavity temperature, and magnetic field strength. These parameters were carefully optimized to ensure stable and consistent mm-wave output. During experimental measurements, the cathode voltage was set to 23.6 kV, with the beam current maintained at 150 mA by adjusting the filament current to approximately 2 A through PID control. The mm-wave frequency is tuned by adjusting the cavity temperature, with adjustments ranging from 10°C to 67.5°C. Furthermore, the frequency can be tuned to higher values by reducing the cathode voltage to 21.5 kV, as demonstrated in the main text Figure 2.

c. Room requirements

The chiller water is provided by a custom-built Haskris Chiller, capable of delivering a flow rate of 64 liters per minute to supply water for the four Sumitomo compressors and one SMC chiller. The ULT system requires a power supply of 50 A at 208 V. Each of the four compressors requires a 208 V – 50 A output. All instruments are backed up by an uninterrupted power supply (UPS). The Sumitomo compressor, Haskris Chiller and SMC chiller were located in a separated room, which reduce the noise for user.

d. Top-loading System

Recently, a sample exchange capability under low temperatures was added to the probe through a top-loading system, allowing for more efficient cooling and reduced waiting time for sample exchange. The top-loading system includes a control system, a sample catcher, a vacuum buffer tank, a diaphragm dry vacuum pump, a rotary valve actuator switch, a transfer line, and an adaptor at the top of the probe outer jacket. The interconnection of each component in the top-loading system is illustrated in the accompanying diagram and described in Figure S1.

The outer jacket of the DNP ULT probe is connected to the sample catcher via the transfer line which contains a rotary valve actuator. The control system includes a vacuum gauge to monitor the pressure of the buffer tank, which is vacuumed by the diaphragm dry vacuum pump. Another vacuum/pressure gauge monitors the pressure from the sample catcher to the probe. The top-loading system facilitates successful loading of rotors into the probe at 35 K and ejection of rotors out of the probe at 90 K.

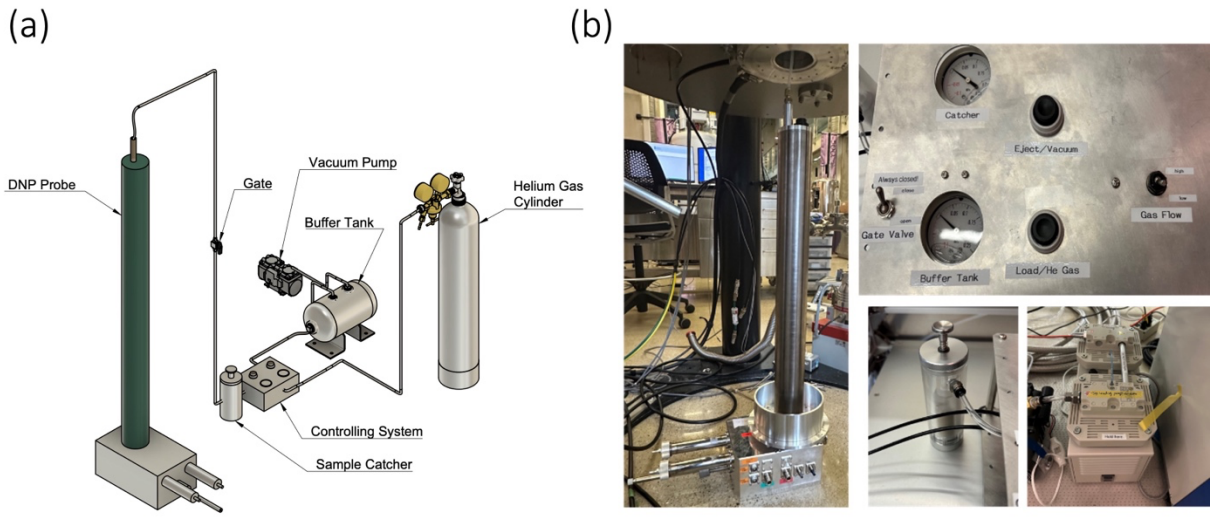

Figure S1: (a) The scheme of top-loading system and (b) the photos of DNP probe with outer jacket, top-loading controlling system, sample catcher and diaphragm vacuum pump.

To insert a new rotor, the DNP probe is first cooled down to 35 K. Then, the rotor is placed into the sample catcher. The sample catcher and the transfer line before the gate are purged with the vacuum pump and refilled with He gas 15 times. After purging, the gate is opened, and the rotor is inserted into the probe by filling it with He gas. After insertion, the gate is immediately closed to avoid exposure to air. Similarly, the rotor can be ejected from the probe when the probe is warmed up to 90 K by vacuuming the transfer line when the gate is open. The rotor is caught by the sample catcher.

e. Relation between gyrotron frequency and cavity temperature

The frequency response of the gyrotron to its cavity temperature was measured twice at different dates (on July 18th and September 3rd, 2024), using the measurement device described above. In both cases, the temperature of the cavity was stepped from low to high temperature, letting the cavity stabilize during 10 min before recording the frequency. The two calibration curves yielded slightly different results. Figure S2 shows that a linear regression fits the first calibration data set well with R_2 = 0.9994, with randomly dispersed residuals. The calibration second data set is not fit well by the linear regression (R_2 = 0.998) and the residuals show a clear trend. Adding a quadratic correction makes the fit better R_2 = 0.9997, with a less pronounced trend of the residuals.

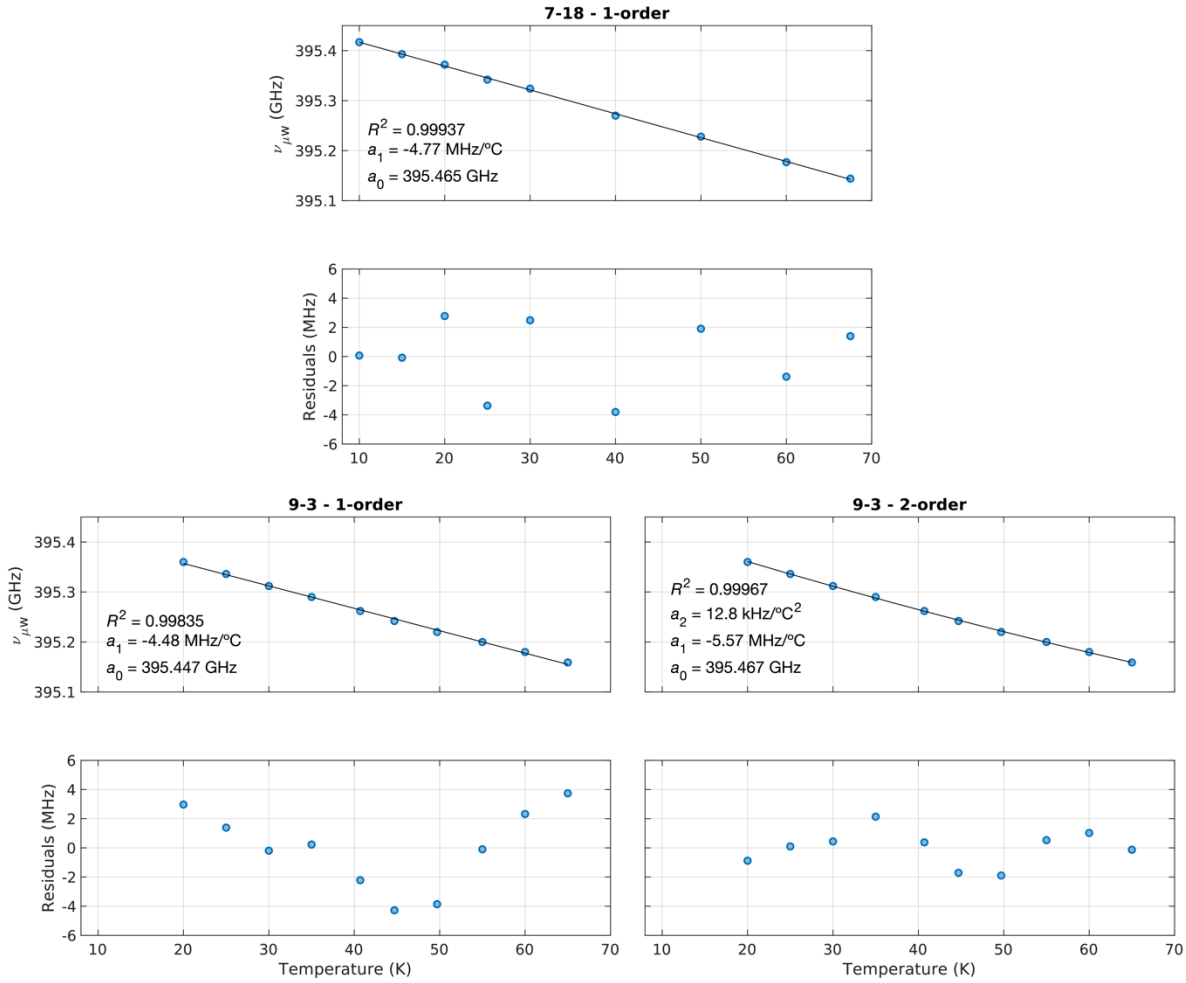

Figure S2: Linear regression of the frequency vs. temperature data set acquired on July 18th, and linear and quadratic regression of the data set acquired on September 3rd. The values a_0, a_1, and a_2 on the plots are the polynomial coefficients of the fits where the index indicates the order of the term associated with it.

Because we found that the relation between temperature and frequency was subject to variation over time, we recorded the DNP profiles monitoring the frequency at multiple points along the acquisition of the profile to be able to correct for possible drifts. During the acquisition of five different DNP profiles, the mm-wave frequency was measured at a total of 57 temperatures. We used this data set and compared it against the prediction of the calibration curves of Figure S2. Figure S3 shows the deviation between the experiment and predicted frequency $\nu_{exp} - \nu_{cal}$, for the 57 measurements and the three calibration curves of Figure S2. The root mean square error (RMSE) on the prediction by each calibration (which corresponds to the root mean square of the data points on the plot) is shown on each plot. The RMSE of the prediction using the quadratic calibration curve obtained from the data set of September 3rd is equal to 2.8 MHz, which is about twice smaller than for the two other calibration curves. Furthermore, the deviations for this calibration curve does not show a clear trend as they do for the two other curves. We therefore chose to use the quadratic calibration curve to compute the frequency in the DNP profile shown in this work. The RMSE of 2.8 MHz is the result of the uncertainty on both the gyrotron frequency and the frequency

measurement. It therefore sets an upper bound for the standard deviation of the mm-wave frequency produced by the gyrotron.

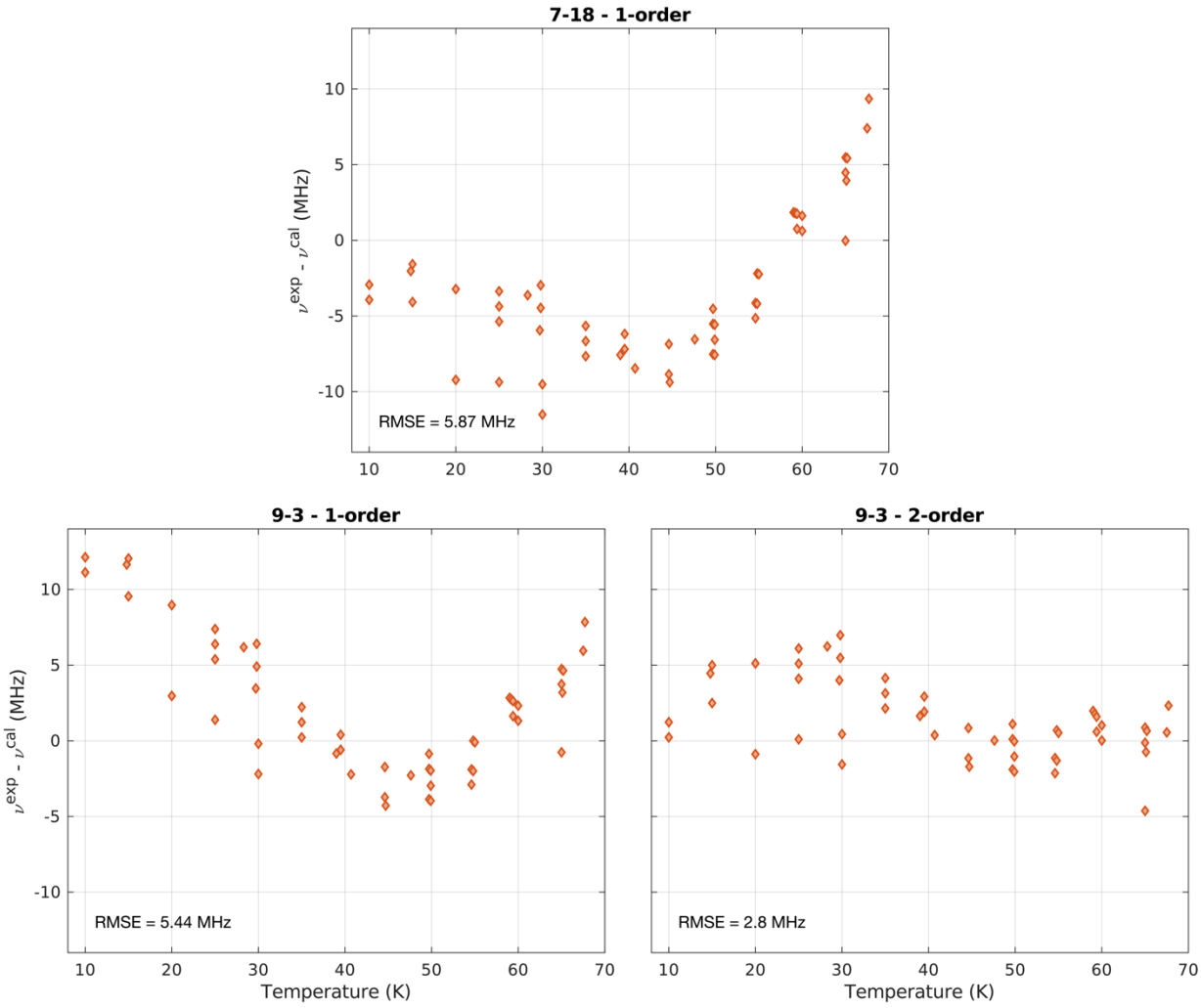

Figure S3: Difference between the measured mm-wave frequency ν_{exp} and the frequency calculated ν_{cal} using the three calibration curves of Figure S2. The measured mm-wave frequencies correspond to a data set of 57 temperature – frequency pairs obtained during the course of five individual DNP profiles.

2. Experimental results

a. Saturation Recovery T_1 and T_{DNP} measurements

Saturation recovery measurements were acquired for the microdiamond sample presented in the main text, using the pulse sequence and parameters described in the Methods sections, for both mm-wave-on and -off conditions. T_1 and T_{DNP} measurements were processed using the DNPLab Python package of data taken from the JEOL Delta software. The FIDs were left-shifted to remove the initial filter signal and Fourier transformed using zero-filling to 1226 points. The single ^{13}C NMR signal of diamond was then integrated by summing the spectrum intensity on a window of 23 ppm. The signal integrals along time t were fitted with a stretched exponential model

$$M(t) = M_\infty - (M_\infty - M_0)\exp\left(-\left(\frac{t}{T}\right)^\beta\right), \quad \text{Eq. S1}$$

where T and β are build-up time constant (T_1 and T_{DNP}, for mm-wave-off and -on measurements, respectively) and the stretch factor between 0 and 1, respectively. The average build-up time constant was obtained as

$$T^{av} = \frac{T}{\beta}\Gamma\left(\frac{1}{\beta}\right), \quad \text{Eq. S2}$$

where Γ is the gamma function.

RT saturation recovery experiments were acquired using 6 kHz MAS both without (Fig. S4a) and with mm-wave irradiation at 395.2015 GHz (positive enhancement peak, Fig. S4b) and 395.366 GHz (negative enhancement peak, Fig. S4c) to obtain the T_{DNP} and T_1 constants, respectively. These curves were subsequently fitted using Eq. S1, giving mean values of T_1^{av} = 780 s, T_{DNP}^{av} (395.2015 GHz) = 608 s, and T_{DNP}^{av} (395.366 GHz) = 468 s, with the fit parameters detailed in Table S1. Because $T_{DNP}^{av} < T_1^{av}$ the on/off enhancements $\epsilon_{on/off}$ of the DNP profiles in Figure 3 only coincide with the absolute enhancements for very long delay times τ between saturation and acquisition, on the order of ~10^3 s. Using the saturation recovery experiments of the mm-wave-on and -off experiments, we computed the absolute and on/off enhancements (see Eqs. 1 and 2) at both delay t = 60 s and as t approaches infinity.

T_1 saturation recovery measurements were also performed at RT under static conditions (Fig. S4d) and at 100 K (Fig. S4e) and 35 K (Fig. S4f) under MAS conditions. Under static RT conditions T_1 was fit with and T_1^{av} = 136 s, and at 100 K and 35 K with 5 kHz MAS the T_1 was fit with and T_1^{av} = 5553 s and 5207 s, respectively. We note that the fits at 100 and 35 K only give an order-of-magnitude estimate due strong noise of the saturation recovery at these temperatures, which is probably due to instabilities in the MAS rate at ULT introducing T_1 noise over the course of the hours-long experiment

Table S1. Saturation recovery curve fittings using a stretched exponential fit (see Eq. S1), where the average time constant is calculated using the gamma function distribution (see Eq. S2). mm-wave-on measurements indicated by (+) and (-) correspond to irradiation at 395.2015 and 395.355 GHz, respectively. The measured values at ULT are only rough estimates so they are given in parenthesis.

Temperature (K)	MAS frequency (kHz)	mm-wave irradiation	Stretched exponential fit		
			$T_{1/DNP}^{av}$ (s)	$T_{1/DNP}$ (s)	Stretch factor β
298	0	off	136	96.2	0.63
298	6	off	780	463	0.55
100	5	off	(5553)	(2610)	(0.48)
35	5	off	(5207)	(816)	(0.33)
298	6	on (+)	608	445	0.65
298	6	on (-)	468	337	0.64

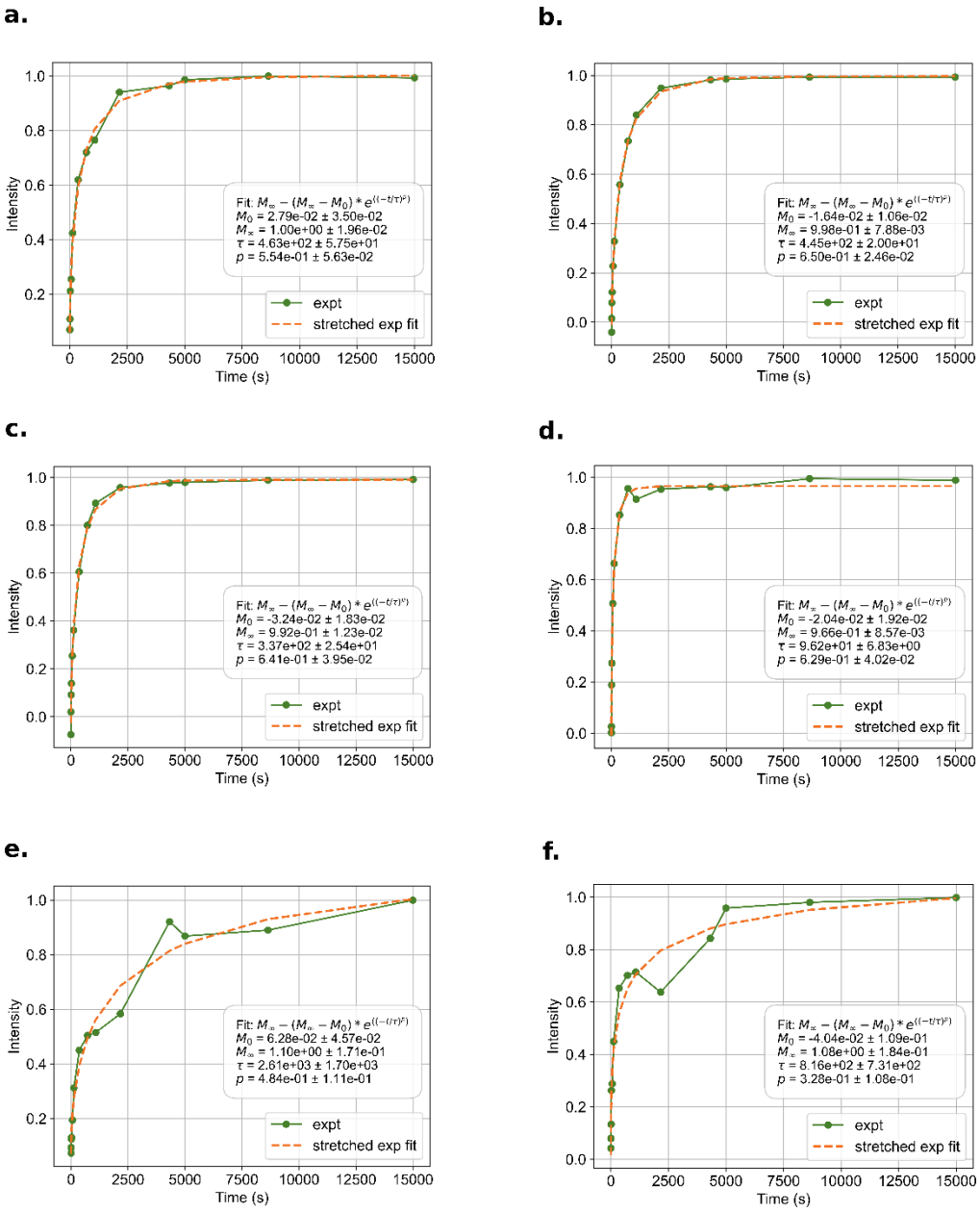

Figure S4: Saturation recovery experiments taken at various conditions. **a**-**d**. are each taken at RT, with (a) at mm-wave-off MAS condition, **b**. at mm-wave-on at the positive DNP enhancement peak (395.2015 GHz), **c.** at mm-wave-on on at the negative DNP enhancement peak (395.366 GHz), and (d) at mm-wave-off Static Condition. **e**. is taken at 100 K at mm-wave-off MAS condition while **f.** is taken at 35 K at mm-wave-off MAS condition. All are fitted using the stretched exponential function with fit parameters and equation shown on each plot.

b. DNP profiles at room temperature on other HPHT diamonds samples

DNP profiles were acquired for three HPHT diamond samples manufactured by Hyperion with different P1 concentrations (10-20, 100, and 100's of ppm) and a size of 100 µm, using the same experimental procedure as for those in the main text of the paper. The normalized DNP profiles are shown in Figure S5. The DNP profiles in absolute value are shown in the inset.

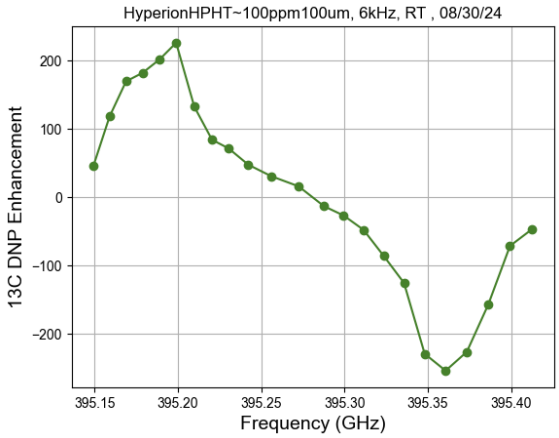

Figure S5: DNP profile for HPHT diamonds by Hyperion.

3. Theory

a. Electron polarization

The electron polarization at thermal equilibrium is calculated using Boltzmann's law

$$P_0 = \tanh\left(\frac{\hbar|\omega_0|}{2K_B T}\right) = \tanh\left(\frac{\mu_B B_0 |g|}{2K_B T}\right), \qquad \text{Eq. S3}$$

where $\hbar$, ω_0, K_B, T, μ_B, B_0, and g are the reduced Planck constant, the Larmor frequency of the electron, Boltzmann's constant, the lattice temperature, Bohr's magneton, the static magnetic field strength, and the g-factor of the electron, respectively. The polarization varies along the EPR spectrum, but a single value can be approximated using the isotropic g-factor.

b. Hole burning models

This section presents the two approaches that were used in this work to simulate hole burning, i.e., the behavior of the EPR line under saturation by mm-wave irradiation: Vega's electron spectral diffusion model (eSD)[62,63] and an analytical solution to the diffusion equation, based on recent work by Wenckebach.[61] In both cases, three mechanisms influence electron spin polarization: mw-wave irradiation, T_{1e} relaxation, and spectral diffusion. Only electron Zeeman order is explicitly accounted for (electron spin dipolar order is neglected). The influence of ^{13}C nuclear spins on the electron spin dynamics is neglected. These models were developed in the context of static DNP and do not account for MAS. They should therefore be seen as phenomenological.

Vega's eSD model: In Vega's model, the EPR line is divided into N bins with frequencies ω_k and intensities f_k for which the electron spin polarization $P(\omega_k)$ is assumed to be homogeneous. The intensity of the line is normalized so that $\sum_{k=1}^{N} f_k = 1$. This model was presented in several publications. The form described here is closest to that presented in Ref. [62,63]. However, we have found some small mistakes and typos in the publications (eg: missing $\hbar$ in a Boltzmann factor and signs) that we attempted to correct in this work.

The shape of the EPR line under saturation by mm-wave irradiation at the steady-state is obtained by solving numerically the differential equation

$$\frac{d}{dt}\vec{P}(t) = (\boldsymbol{W}_{\mathrm{mw}} + \boldsymbol{R}_1 + \boldsymbol{R}_{\mathrm{D}})\vec{P}(t), \qquad \text{Eq. S4}$$

where $\vec{P}(t) = [1, P_1, P_2, \ldots, P_N]^{\mathrm{T}}$ is a vector representing the polarizations in the N bins. The first unity term in the vector allows to compute relaxation while keeping the differential equation homogeneous. The three matrices $\boldsymbol{W}_{\mathrm{mw}}$, $\boldsymbol{R}_1$, and $\boldsymbol{R}_{\mathrm{D}}$ acting on the polarization vector represent mm-wave irradiation, $T_{1\mathrm{e}}$ relaxation, and spectral diffusion, respectively. We did not include the DQ and ZQ SE transitions assuming that they are weak in our experimental conditions. $\boldsymbol{W}_{\mathrm{mw}}$ represents the saturation of the single quantum transitions and only contains non-zero elements on the diagonal, which can be represented as

$$(\boldsymbol{W}_{\mathrm{mw}})_{kk} = -\frac{\omega_1^2 T_2}{1+(\omega_k-\omega_{\mathrm{mw}})^2 T_2^2}, \qquad \text{Eq. S5}$$

where ω_1, T_2, ω_k, and ω_{mw} are the strength of the mm-wave field in rad.s^{-1}, the electron spin-spin relaxation time constant, the electron spin resonance frequency of bin k, and the mm-wave frequency, respectively. The action of $\boldsymbol{R}_1$ can be represented in the subspace of electron spin k as

$$\frac{d}{dt}\begin{pmatrix}1\\P_k(t)\end{pmatrix} = \begin{pmatrix}0 & 0\\ \frac{P_{0,k}}{T_1} & -\frac{1}{T_1}\end{pmatrix}\begin{pmatrix}1\\P_k(t)\end{pmatrix}, \qquad \text{Eq. S6}$$

where $T_{1,k} = T_{1\mathrm{e}}$ is assumed to be constant across the EPR line and $P_{0,k}$ is the Boltzmann polarization for bin k, calculated by setting $\omega_0 = \omega_k$ in Eq. S3. The non-zero matrix elements of $\boldsymbol{R}_1$ can therefore be written as

$$(\boldsymbol{R}_1)_{k1} = \frac{P_{0,k}}{T_1}, \qquad \text{Eq. S7}$$

$$(\boldsymbol{R}_1)_{kk} = -\frac{1}{T_1}.$$

Finally, $\boldsymbol{R}_{\mathrm{D}}$, which represents spectral diffusion, is the only matrix with non-diagonal terms, which connects bins with each other. It can be represented as the sum

$$\boldsymbol{R}_{\mathrm{D}} = \sum_{j>k} \boldsymbol{R}_{\mathrm{D},kj}, \qquad \text{Eq. S8}$$

of matrices in the subspace of electron spin k and j,

$$\boldsymbol{R}_{\mathrm{D},kj} = \frac{\Lambda^{\mathrm{eSD}}}{(\omega_k-\omega_j)^2}\frac{1}{1+\eta_{kj}}\begin{pmatrix}-\eta_{kj}f_j & +f_j\\ +\eta_{kj}f_k & -f_k\end{pmatrix}, \qquad \text{Eq. S9}$$

where Λ^{eSD}, f_k and f_j are a coefficient describing the efficiency of spectral diffusion in s^{-3} and the normalized EPR intensities of bins k and j, respectively. The thermal correction factor

$$\eta_{kj} = \frac{P_{0,j}}{P_{0,k}}, \qquad \text{Eq. S10}$$

ensures that spectral diffusion preserves the gradient of polarization at Boltzmann equilibrium that arises from the difference in Larmor frequency of the individual spin packets. Note that the thermal correction factor in Eq. S10 is defined in this way in Ref. [62]. An alternative form of this term is given in several other references by the same group (eg, Ref. [63,64,73]), which is based on Boltzmann factors

$$\eta_{kj} = \exp\left(-\frac{\hbar}{K_{\mathrm{BT}}}(\omega_k - \omega_j)\right). \qquad \text{Eq. S11}$$

According to Eq. 16b in Ref. [73] and Eq. 69 in Ref. [64], the expression in Eq S11 is supposed to be equal to that in Eq. S10. However, these equations are in fact not equal; the proposed Boltzmann factor gives a

population ratio, and not a polarization ratio as in Eq. S10. We performed test simulation of the eSD model switching off mm-wave saturation (that is, setting $\omega_1 = 0$). In this case, only spectral diffusion is active. If the thermal correction factor is correct, the polarization across the EPR line, should remain constant at all times. We found that Eq. S10 did produce the appropriate gradient of polarization (as predicted by Eq. S3), while not Eq. S11 (see Figure S6). We therefore chose to use Eq. S10.

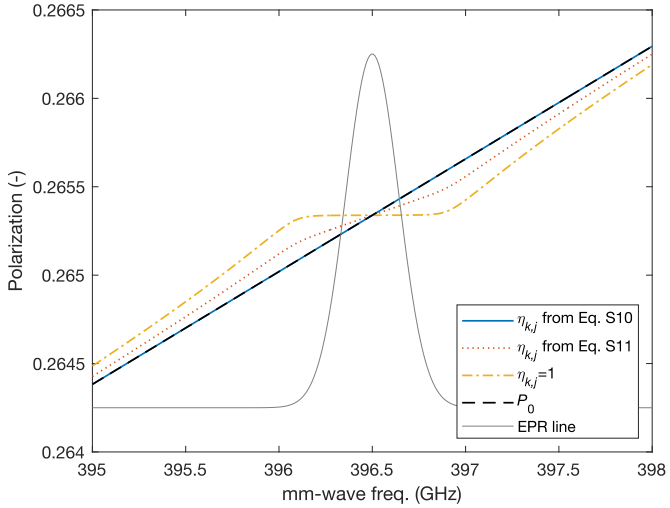

Figure S6: Verification of the validity of the thermal correction factor given in Eq. S10. The polarization as a function of frequency is simulated using the eSD (see Eq. S4) for a Gaussian EPR line with standard deviation of 100 MHz centered at 396.5 GHz (represented by a grey line in arbitrary units), with no mm-wave irradiation ($\omega_1 = 0$), T_2 = 1 µs (which does not influence the simulation because $\omega_1 = 0$), T_1 = 1 ms, and Λ^{eSD} = 4000 µs^{-3}. The black dashed line represents the initial polarization, computed using Eq. S3. The blue, red dotted, and yellow dashed dotted lines represent the final polarization (at $t_{max} = 5 \cdot T_{1e}$ = 5 ms) if the thermal correction factor is computed using Eq. S10, using Eq. S11, or set to 1, respectively.

In all cases, we used the differential equation solver of MATLAB *ode15s*, which is optimized for problems with timescales ranging on different orders of magnitude. The differential equation was solved on a time range from 0 to $t_{max} = 5 \cdot T_{1e}$. The last vector $\vec{P}(t_{max})$ computed by *ode15s* was assumed to represent the electron spin polarization at dynamic equilibrium.

Analytical solution to the spectral diffusion equation: An alternative to Vega's eSD is to treat spectral diffusion as a standard 1-dimensional diffusion equation. A difficulty that arises in this case is how to obtain the frequency dependence of the diffusion coefficient. Wenckebach recently proposed an approach based on Monte Carlo simulation.[61] Here, we use a simple approximation of the diffusion equation where the diffusion coefficient is assumed to be constant across the EPR line, as proposed by Vaneeckhaute *et al*.[60] This approach has the advantage of yielding an analytical solution with a limited number of free parameters. Under the assumption of constant T_{1e} and diffusion coefficient D across the EPR line, the diffusion equation can be expressed as

$$\frac{\partial}{\partial t}P(\nu) = -\pi\omega_1^2\, h\big(\omega - \omega_{\mu w}\big)P(\omega) + D\frac{\partial^2}{\partial \omega^2}P(\omega) + \frac{P_0 - P(\omega)}{T_{1e}}, \qquad \text{Eq. S12}$$

where *h* and *D* are the homogeneous broadening and the spectral diffusion coefficient, respectively. If we further assume that the homogeneous broadening is small compared to the inhomogeneous broadening, the mm-waves are only on resonance with spins of the exact same frequency. Eq. S12 then becomes

$$\frac{\partial}{\partial t}P(\omega) = -\pi\omega_1^2\, P(\omega)\delta(\omega - \omega_{\mathrm{mw}}) + D\,\frac{\partial^2}{\partial\omega^2}P(\omega) + \frac{P_0 - P(\omega)}{T_{1\mathrm{e}}}. \qquad \text{Eq. S13}$$

At equilibrium, that is, when Eq. S13 is null, the diffusion equation has the solution

$$P_{\mathrm{mw}}(\omega) = P_0\left(1 - \exp\left(-\frac{|\omega - \omega_{\mathrm{mw}}|}{\Lambda}\right)\right), \qquad \text{Eq. S14}$$

where $\Lambda = (DT_{1\mathrm{e}})^{1/2}$ is the spectral diffusion length.

c. DNP model using analytical equations

This section shows the derivation of simple formula for the profiles of the solid effect (SE), the cross effect (CE), and the truncated cross effect (tCE) for the case where spectral diffusion can be neglected. This derivation also requires the hypothesis that the electron spin-lattice relaxation time $T_{1\mathrm{e}}$ is constant across the EPR line, leading to a constant saturation efficiency across the line. Alternatively, assuming full saturation yields the same result. It is further assumed that nuclear spin diffusion averages nuclear polarization across the sample.

Solid effect case: If there is no electron spectral diffusion, the polarization of electron spins on resonance with double- and zero-quantum transitions (DQ and ZQ) are not affected by each other nor they are affected by depolarization of electron spin on resonance with single quantum transition (SQ). In this case, SE affects the nuclear polarization only for nuclear spins interacting with electrons on resonance with the ZQ and DQ transitions, yielding

$$P_{\mathrm{I}}^{\mathrm{SE,ZQ}}(\omega_{\mathrm{mw}} + \omega_{\mathrm{I}}) = -\chi P_0, \qquad \text{Eq. S15}$$

and

$$P_{\mathrm{I}}^{\mathrm{SE,DQ}}(\omega_{\mathrm{mw}} - \omega_{\mathrm{I}}) = +\chi P_0, \qquad \text{Eq. S16}$$

where ω_{I}, χ, and P_0 are the absolute value of the nuclear Larmor frequency, a factor describing the dynamic efficiency of the saturation of the SE transitions, and the electron polarization at Boltzmann equilibrium (see Eq. S3), respectively. Assuming that nuclear spin diffusion equalizes polarization across the sample and that the nuclear Boltzmann polarization and nuclear relaxation are negligible, the bulk nuclear polarization is the weighed summed of the two contributions of Eqs. S15 and S16

$$\begin{aligned} P_{\mathrm{I}}^{\mathrm{SE}}(\omega_{\mathrm{mw}}) &= f(\omega_{\mathrm{mw}} + \omega_{\mathrm{I}})P_{\mathrm{I}}^{\mathrm{SE,ZQ}} + f(\omega_{\mathrm{mw}} - \omega_{\mathrm{I}})P_{\mathrm{I}}^{\mathrm{SE,DQ}} \\ &= \chi P_0\big(f(\omega_{\mathrm{mw}} - \omega_{\mathrm{I}}) - f(\omega_{\mathrm{mw}} + \omega_{\mathrm{I}})\big), \end{aligned} \qquad \text{Eq. S17}$$

The shape of the SE profile is then given by Eq. S17, dropping constant factors

$$f_{\mathrm{SE}}(\omega_{\mathrm{mw}}) = f(\omega_{\mathrm{mw}} - \omega_{\mathrm{I}}) - f(\omega_{\mathrm{mw}} + \omega_{\mathrm{I}}), \qquad \text{Eq. S18}$$

which can be obtained concisely as the convolution integral

$$f_{\mathrm{SE}}(\omega_{\mathrm{mw}}) = (f * u)[\omega_{\mathrm{mw}}], \qquad \text{Eq. S19}$$

of the EPR line with the function

$$u(\nu) = \delta(\omega + \omega_I) - \delta(\omega - \omega_I), \qquad \text{Eq. S20}$$

where δ is the Dirac delta function.

Cross effect case: The CE transfers the polarization difference between two electrons to a nuclear spin via triple spin flips, provided the Larmor frequency difference of the two electrons $\omega_1 - \omega_2$ matches the nuclear Larmor frequency ω_I. At equilibrium, a nuclear spin interacting with such a pair of electron spins has polarization[59,74]

$$P_{\mathrm{I}} = \frac{P_1 - P_2}{1 - P_1 P_2}, \qquad \text{Eq. S21}$$

where P_1 and P_2 are the polarizations of the two electron spins. The denominator is a normalization constant that only plays a role at high electron polarization. Assuming that spin diffusion averages the nuclear spin polarization, the bulk nuclear polarization is given by the weighted average over all possible electron spin pairs fulfilling the CE matching condition

$$P_{\mathrm{I}} = \frac{1}{F_{\mathrm{N}}} \int d\omega f(\omega) f(\omega - \omega_{\mathrm{I}}) \frac{P(\omega) - P(\omega - \omega_{\mathrm{I}})}{1 - P(\omega) P(\omega - \omega_{\mathrm{I}})}, \qquad \text{Eq. S22}$$

where $P(\omega)$ is the electron polarization at frequency ω in the EPR line, and the normalization factor condition

$$F_{\mathrm{N}} = \int d\omega f(\omega) f(\omega - \omega_{\mathrm{I}}). \qquad \text{Eq. S23}$$

The term $f(\omega_{\mathrm{I}}) f(\omega - \omega_{\mathrm{I}})/F_{\mathrm{N}}$ in Eq. S22 expresses the probability for a particular pair of electron spins to fulfill the CE matching condition, given the EPR intensities $f(\omega_{\mathrm{I}})$ and $f(\omega - \omega_{\mathrm{I}})$. In absence of mm-wave irradiation, the $P(\omega_{\mathrm{I}}) - P(\omega - \omega_{\mathrm{I}})$ is equal to the nuclear Boltzmann polarization P_{I0} and Eq. S22 predicts $P_{\mathrm{I}} = P_{\mathrm{I0}}$. In this case, CE serves as a T_1 relaxation mechanism for nuclear spins. CE DNP consist of creating an out-of-equilibrium difference between electron spins via mm-wave (or microwave) irradiation that then transfers spontaneously to nuclear spins.

If there is no spectral diffusion, triple spin flips only result in hyperpolarization between the electron spins being saturated (with $\omega = \omega_{\mathrm{mw}}$) and those satisfying $\omega = \omega_{\mathrm{mw}} - \omega_{\mathrm{I}}$ and $\omega = \omega_{\mathrm{mw}} + \omega_{\mathrm{I}}$, on the left and on the right of the irradiation frequency, respectively. In these two cases, Eq. S21 gives the polarization of nuclear spins interacting with such electron spin pairs are

$$P_{\mathrm{I}}^{\mathrm{CE,left}}(\omega_{\mathrm{mw}}) = \frac{P(\omega_{\mathrm{mw}}) - P(\omega_{\mathrm{mw}} - \omega_{\mathrm{I}})}{1 - P(\omega_{\mathrm{mw}}) P(\omega_{\mathrm{mw}} - \omega_{\mathrm{I}})}, \qquad \text{Eq. S24}$$

and

$$P_{\mathrm{I}}^{\mathrm{CE,right}}(\omega_{\mathrm{mw}}) = \frac{P(\omega_{\mathrm{mw}} + \omega_{\mathrm{I}}) - P(\omega_{\mathrm{mw}})}{1 - P(\omega_{\mathrm{mw}}) P(\omega_{\mathrm{mw}} + \omega_{\mathrm{I}})}. \qquad \text{Eq. S25}$$

Because there is no spectral diffusion, the polarization of the left and right partners is that of thermal equilibrium P_0

$$P(\omega_{\mathrm{mw}} - \omega_I) = P(\omega_{\mathrm{mw}} + \omega_{\mathrm{I}}) = P_0, \qquad \text{Eq. S26}$$

and assuming a homogeneous T_{1e} across the EPR line (or that saturation is infinite), the saturation factor is constant across the EPR line, yielding

$$P(\omega_{\mathrm{mw}}) = P^{\mathrm{sat}}. \qquad \text{Eq. S27}$$

We therefore have

$$P_{\mathrm{I}}^{\mathrm{CE,left}}(\omega_{\mathrm{mw}}) = \frac{P^{\mathrm{sat}} - P_0}{1 - P^{\mathrm{sat}} P_0}. \qquad \text{Eq. S28}$$

and

$$P_{\mathrm{I}}^{\mathrm{CE,right}}(\omega_{\mathrm{mw}}) = \frac{P_0 - P^{\mathrm{sat}}}{1 - P_0 P^{\mathrm{sat}}}, \qquad \text{Eq. S29}$$

Hence, the integral of Eq. S22 is the sum of the two terms of Eqs. S28 and S29, with the weights, $f(\omega_{\mathrm{mw}})f(\omega_{\mathrm{mw}} - \omega_{\mathrm{I}})/F_{\mathrm{N}}$ and $f(\omega_{\mathrm{mw}})f(\omega_{\mathrm{mw}} + \omega_{\mathrm{I}})/F_{\mathrm{N}}$, respectively, yielding

$$P_{\mathrm{I}}^{\mathrm{CE}}(\omega_{\mathrm{mw}}) = \frac{f(\omega_{\mathrm{mw}})f(\omega_{\mathrm{mw}} - \omega_{\mathrm{I}})}{F_{\mathrm{N}}} P_{\mathrm{I}}^{\mathrm{CE,left}}(\omega_{\mathrm{mw}}) + \frac{f(\omega_{\mathrm{mw}})f(\omega_{\mathrm{mw}} + \omega_{\mathrm{I}})}{F_{\mathrm{N}}} P_{\mathrm{I}}^{\mathrm{CE,right}}(\omega_{\mathrm{mw}}) \qquad \text{Eq. S30}$$

$$= \frac{1}{F_{\mathrm{N}}} \frac{P_0 - P^{\mathrm{sat}}}{1 - P_0 P^{\mathrm{sat}}} f(\omega_{\mathrm{mw}}) \big(f(\omega_{\mathrm{mw}} + \omega_{\mathrm{I}}) - f(\omega_{\mathrm{mw}} - \omega_{\mathrm{I}}) \big).$$

The shape of the CE profile is then given by Eq. S30, dropping the constant factors

$$f_{\mathrm{CE}}(\omega_{\mathrm{mw}}) = f(\omega_{\mathrm{mw}}) \big(f(\omega_{\mathrm{mw}} + \omega_{\mathrm{I}}) - f(\omega_{\mathrm{mw}} - \omega_{\mathrm{I}}) \big). \qquad \text{Eq. S31}$$

As for the SE, this can be computed in a compact way as a convolution integral (or as the product of the EPR line with the SE profile)

$$f_{\mathrm{CE}}(\omega_{\mathrm{mw}}) = f(\omega_{\mathrm{mw}}) \big((f * u)[\omega_{\mathrm{mw}}] \big) = f(\omega_{\mathrm{mw}}) f_{\mathrm{SE}}(\omega_{\mathrm{mw}}). \qquad \text{Eq. S32}$$

Truncated cross effect case: the tCE without spectral diffusion can be computed in a similar way as the CE. Let us call f_{S} and f_{F} the EPR lineshape of the slow- and fast-relaxing spins, respectively. For the case where spectral diffusion among the slow-relaxing spins can be neglected, triple spin flips leading to nuclear hyperpolarization only occur for the saturated slow-relaxing spin (with $\omega_{\mathrm{S}} = \omega_{\mathrm{mw}}$) and the fast-relaxing spins satisfying $\omega_{\mathrm{F}} = \omega_{\mathrm{mw}} - \omega_{\mathrm{I}}$ and $\omega_{\mathrm{F}} = \omega_{\mathrm{mw}} + \omega_{\mathrm{I}}$. Eqs. S24 and S25 can then be adapted to the tCE as

$$P_{\mathrm{I}}^{\mathrm{tCE,left}}(\omega_{\mathrm{mw}}) = \frac{P_{\mathrm{S}}(\omega_{\mathrm{mw}}) - P_{\mathrm{F}}(\omega_{\mathrm{mw}} - \omega_{\mathrm{I}})}{1 - P_{\mathrm{S}}(\omega_{\mathrm{mw}}) P_{\mathrm{F}}(\omega_{\mathrm{mw}} - \omega_{\mathrm{I}})}, \qquad \text{Eq. S33}$$

and

$$P_{\mathrm{I}}^{\mathrm{tCE,right}}(\omega_{\mathrm{mw}}) = \frac{P_{\mathrm{F}}(\omega_{\mathrm{mw}} + \omega_{\mathrm{I}}) - P_{\mathrm{S}}(\omega_{\mathrm{mw}})}{1 - P_{\mathrm{S}}(\omega_{\mathrm{mw}}) P_{\mathrm{F}}(\omega_{\mathrm{mw}} + \omega_{\mathrm{I}})}. \qquad \text{Eq. S34}$$

Assuming that fast-relaxing spins are always at Boltzmann polarization P_0 and writing $P_{\mathrm{S}}(\omega_{\mathrm{mw}}) = P^{\mathrm{sat}}$, we have

$$P_{\mathrm{I}}^{\mathrm{tCE,left}}(\omega_{\mathrm{mw}}) = \frac{P^{\mathrm{sat}} - P_0}{1 - P^{\mathrm{sat}} P_0}, \qquad \text{Eq. S35}$$

and

$$P_{\mathrm{I}}^{\mathrm{tCE,right}}(\omega_{\mathrm{mw}}) = \frac{P_0 - P^{\mathrm{sat}}}{1 - P^{\mathrm{sat}} P_0}. \qquad \text{Eq. S36}$$

Hence, the

$$P_{\mathrm{I}}^{\mathrm{tCE}}(\omega_{\mathrm{mw}}) = \frac{f_{\mathrm{S}}(\omega_{\mathrm{mw}})f_{\mathrm{F}}(\omega_{\mathrm{mw}}-\omega_{\mathrm{I}})}{F_{\mathrm{N}}} P_{\mathrm{I}}^{\mathrm{tCE,left}}\left(\omega_{\mu\mathrm{w}}\right) + \frac{f_{\mathrm{S}}(\omega_{\mathrm{mw}})f_{\mathrm{F}}(\omega_{\mathrm{mw}}+\omega_{\mathrm{I}})}{F_{\mathrm{N}}} P_{\mathrm{I}}^{\mathrm{tCE,right}}(\omega_{\mathrm{mw}})$$

$$= \frac{1}{F_{\mathrm{N}}} \frac{P_0 - P^{\mathrm{sat}}}{1 - P^{\mathrm{sat}} P_0} f_{\mathrm{S}}(\omega_{\mathrm{mw}})\left(f_{\mathrm{F}}(\omega_{\mathrm{mw}} + \omega_{\mathrm{I}}) - f_{\mathrm{F}}(\omega_{\mathrm{mw}} - \omega_{\mathrm{I}})\right), \qquad \text{Eq. S37}$$

where the normalization factor is defined as

$$F_{\mathrm{N}} = \int d\omega f_{\mathrm{S}}(\omega)\left(f_{\mathrm{F}}(\omega + \omega_{\mathrm{I}}) + f_{\mathrm{F}}(\omega - \omega_{\mathrm{I}})\right). \qquad \text{Eq. S38}$$

The shape of the tCE profile is then given by Eq. S38, dropping constant factors

$$f_{\mathrm{tCE}}\left(\nu_{\mu\mathrm{w}}\right) = f_{\mathrm{S}}(\omega_{\mathrm{mw}})\left(f_{\mathrm{F}}(\omega_{\mathrm{mw}} + \omega_{\mathrm{I}}) - f_{\mathrm{F}}(\omega_{\mathrm{mw}} - \omega_{\mathrm{I}})\right). \qquad \text{Eq. S39}$$

In the case where the fast-relaxing are shifted from the slow-relaxing by approximately ω_{I} (i.e., resonance-matched), only one of the two terms $f_{\mathrm{F}}(\omega_{\mathrm{mw}} + \omega_{\mathrm{I}})$ and $f_{\mathrm{F}}(\omega_{\mathrm{mw}} - \omega_{\mathrm{I}})$ is non-zero. Furthermore, if the resonance of the fast-relaxing spins is broad compared to the slow-relaxing spins, the value of f_{F} in the one term that is non-zero can be considered constant over the range where $f_{\mathrm{S}}(\omega_{\mathrm{mw}})$ is non-zero. Then, we have either

$$f_{\mathrm{tCE}}(\omega_{\mathrm{mw}}) \approx +f_{\mathrm{S}}(\omega_{\mathrm{mw}}), \qquad \text{Eq. S40}$$

or

$$f_{\mathrm{tCE}}(\omega_{\mathrm{mw}}) \approx -f_{\mathrm{S}}(\omega_{\mathrm{mw}}), \qquad \text{Eq. S41}$$

whether the fast-relaxing spins are shifted by $+\omega_{\mathrm{I}}$ or $-\omega_{\mathrm{I}}$ with respect to the EPR line of the slow-relaxing spins, respectively. In this case, the DNP profile has the same shape as the EPR line, up to a sign, as is the case for the Overhauser effect.

d. DNP model including spectral diffusion

To include spectral diffusion in the simulations of the CE and tCE, one must consider the triple flips of the nucleus with all pairs of electrons spins fulfilling the CE matching conditions, not only on resonance with the mm-waves. In the case of the CE, the sum can be written as

$$P_{\mathrm{I}}^{\mathrm{CE}}(\omega_{\mathrm{mw}}) = \frac{1}{F_{\mathrm{n}}} \sum_{k=1}^{N} f(\omega_k) f(\omega_k + \omega_{\mathrm{I}}) \frac{P_{\mathrm{mw}}(\omega_k+\omega_{\mathrm{I}}) - P_{\mathrm{mw}}(\omega_k)}{1 - P_{\mathrm{mw}}(\omega_k+\nu_{\mathrm{I}}) P_{\mathrm{mw}}(\omega_k)}, \qquad \text{Eq. S42}$$

where N is the number of bins in the EPR spectrum, and the normalization factor is

$$F_{\mathrm{n}} = \sum_{k=1}^{N} f(\omega_k) f(\omega_k + \omega_{\mathrm{I}}). \qquad \text{Eq. S43}$$

Note that it is not necessary to account for triple-spin flips on the left and right, as they are both covered by the summation. In the case of the tCE, the integration yields

$$P_{\mathrm{I}}^{\mathrm{tCE}}(\omega_{\mathrm{mw}}) = \frac{1}{F_{\mathrm{n}}} \sum_k \left(f_{\mathrm{S}}(\omega_k) f_{\mathrm{F}}(\omega_k - \omega_{\mathrm{I}}) \frac{P_0 - P_{\mathrm{S}}^{\mathrm{mw}}(\omega_k)}{1 - P_0 P_{\mathrm{S}}^{\mathrm{mw}}(\omega_k)} + f_{\mathrm{S}}(\omega_k) f_{\mathrm{F}}(\omega_k + \omega_{\mathrm{I}}) \frac{P_{\mathrm{S}}^{\mathrm{mw}}(\omega_k) - P_0}{1 - P_0 P_{\mathrm{S}}^{\mathrm{mw}}(\omega_k)} \right), \qquad \text{Eq. S44}$$

where N is the number of bins in the EPR spectrum, and the normalization factor is

$$F_{\mathrm{n}} = \sum_{k=1}^{N} \left(f_{\mathrm{S}}(\omega_k) f_{\mathrm{F}}(\omega_k - \omega_{\mathrm{I}}) + f_{\mathrm{S}}(\omega_k) f_{\mathrm{F}}(\omega_k + \omega_{\mathrm{I}}) \right). \qquad \text{Eq. S45}$$

4. Simulation results

a. P1 EPR line

Figure S7 shows the simulated EPR line at 14.1 T as in the main text of the paper (black line) together with the contributions of the different P1 populations.

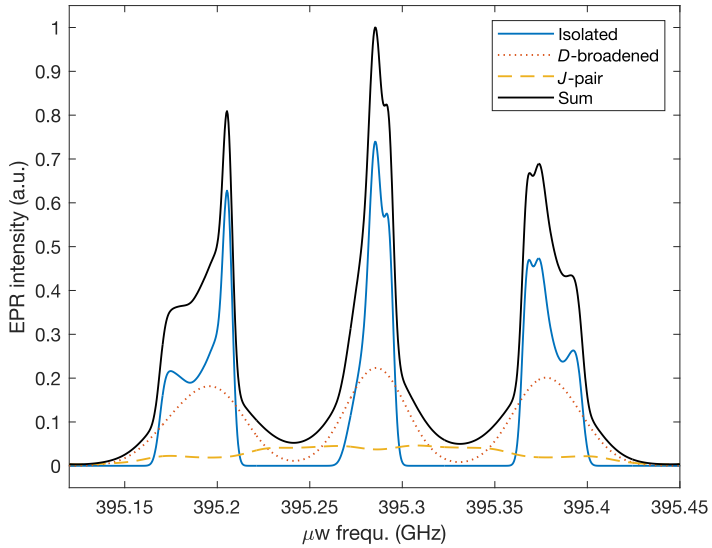

Figure S7: Simulation of the EPR line using *Easyspin's* function *pepper* for solid-state powder averaging. The summed spectrum (in black) is decomposed into three contributions (isolated, dipolar-broadened, and exchange-coupled pairs). See the Methods section for details on the simulation parameters.

b. DNP profiles with different hole burning models

The DNP profiles were simulated for P1 spins at 14.1 T as a linear combination

$$f(\omega_{\mathrm{mw}}) = x_{\mathrm{tCE}} f_{\mathrm{tCE}}(\omega_{\mathrm{mw}}) + (1 - x_{\mathrm{tCE}}) f_{\mathrm{CE}}(\omega_{\mathrm{mw}}), \qquad \text{Eq. S44}$$

where x_{tCE} is contribution of the tCE profile between 0 and 1, using Eqs. S42 and S44. The polarization of the slow-relaxing P1 spins as function of frequency $P_S^{\mathrm{mw}}(\omega_k)$ was computed using both hole burning models presented in Section 3b. In both cases, it was assumed that dipolar-broadened and exchange-coupled P1 spins play the role of slow- and fast-relaxing partners. Figure S8 shows the simulated DNP profiles using Vega's eSD model (see Eq. S4) and the analytical solution to the diffusion equation (see Eq. S14), in panel a and b, respectively. For the eSD model, 11 free parameters were manually fit to the experimental data: x_{tCE}, T_1 (individually for set of experimental conditions), T_2, ω_1, and Λ^{eSD}, respectively, (the last three being kept constant for all conditions). For the analytical model, the only fit parameters were x_{tCE} and the spectral diffusion length Λ. Table S2 summarizes the fit results. The digitization of the EPR spectrum was set to a low value for the eSD model (as represented by dots on the EPR lines of the bottom plots of Figure S8a) to fulfill the condition[62] that the frequency difference between the bins (8 MHz) does not exceed the homogeneous broadening: ω_{k+1} - ω_k > $2/T_2$ (8 MHz). In the case of the analytical model, there is requirement regarding the frequency separation between the bins.

Table S2: Fit parameters of the spectral diffusion/hole burning models used to compute the DNP profiles shown in Figure S8.

Vega's eSD model				
T (K)	298, Static	298, MAS	100	35
x_{tCE}	0.5	0.5	0.5	0.5
T_1 (ms)	0.12	0.12	4	5
T_2 (ns)	40			
$\omega_1/2\pi$ (kHz)	300			
Λ^{eSD} (μs^{-3})	800			

Analytical model				
T (K)	298, Static	298, MAS	100	35
x_{tCE}	0.6	0.6	0.7	0.7
Λ (MHz)	22	20	130	130

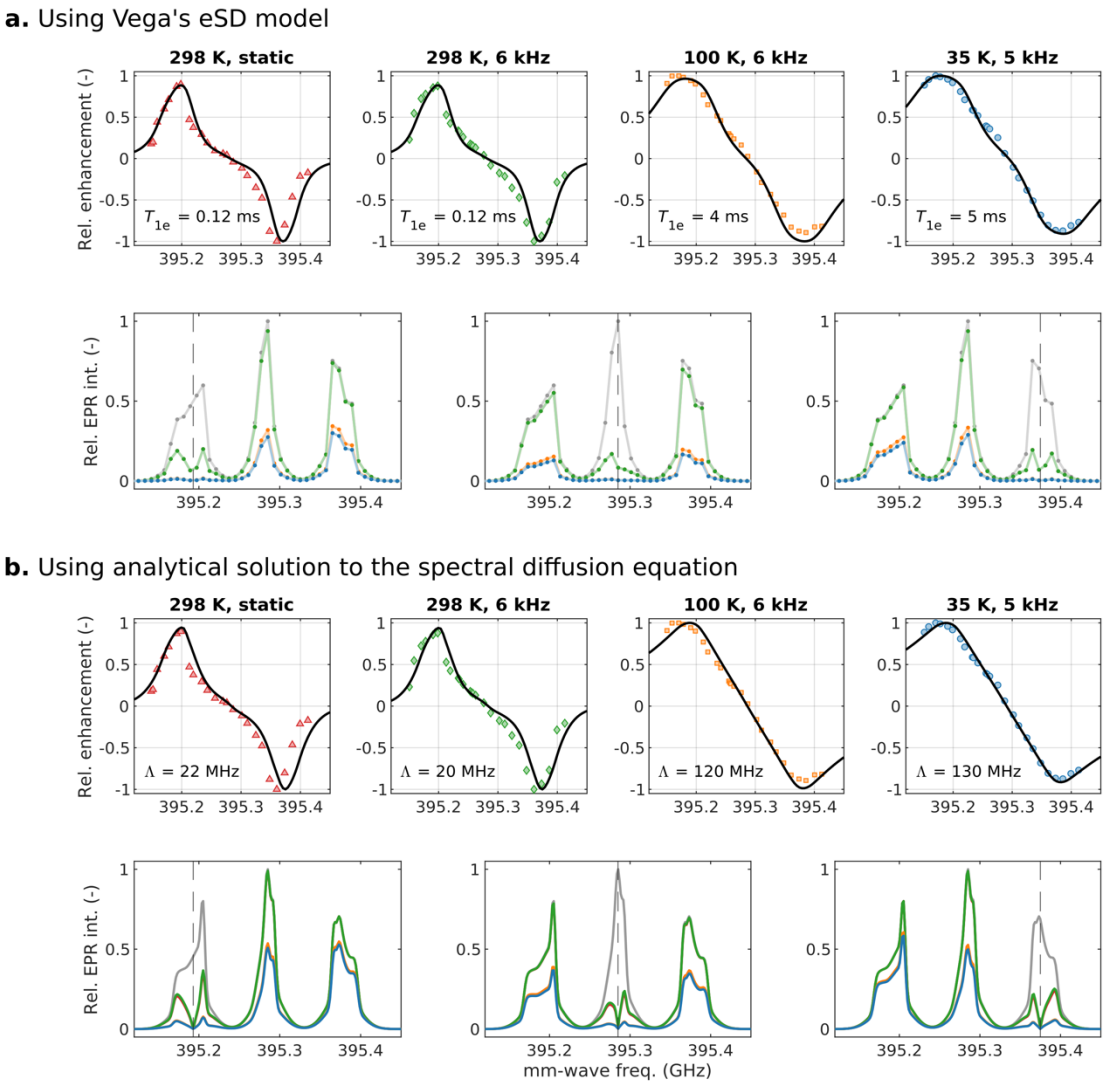

Figure S8: Computation of the simulated DNP profiles using Eqs. S42 and S44 and the Vega's eSD model (see Eq. S4) and the analytical solution to the diffusion equation (see Eq. S14), panel a and b, respectively. In each panel, the top row represents the normalized experimental DNP profiles (colored symbols) and the model (black lines). The bottom

row represents the EPR line of the slow-relaxing spins under saturation (colored lines) compared with that at thermal equilibrium (grey lines), for three different mm-wave frequencies (represented by vertical dashed lines).

Table S3: Separation between the positive and negative DNP optima in the experimental profiles Δ_{exp}, compared with that of the simulated profiles Δ_{sim} (simulated using the analytical solution to the diffusion equation), and the profiles of the tCE and CE contributions, Δ_{tCE} and Δ_{CE}, respectively, for the simulation using the analytical solution to the diffusion equation.

T (K)	Δ_{exp}	Δ_{sim}	Δ_{tCE}	Δ_{CE}
298, static	162	175	188	150
298, MAS	162	175	184	150
100	215	188	196	163
35	215	196	196	163

c. SE-DNP simulation

Figure S9 shows the simulated DNP profile for the SE (in gray) using Eq. S19 and the entire EPR line (isolated, dipolar-broadened, and exchange-coupled spins) compared with the experimental results in all experimental conditions (colored symbols).

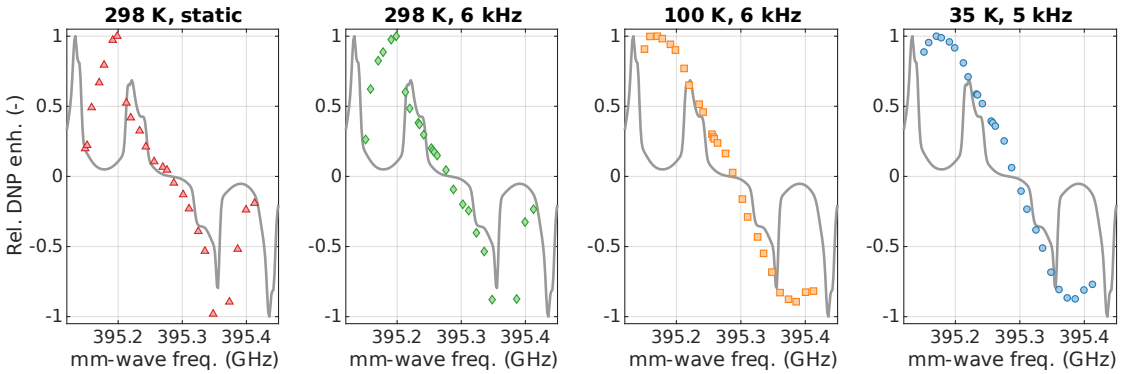

Figure S9: SE simulation using Eq. S19 (gray line), compared with the experimental data (colored dots).

d. Prediction of the DNP profiles at 3.3 and 6.9 T

The ^{13}C-DNP profiles acquired at 3.3 and 6.9 T and room temperature for the same diamond sample were reported in Ref. [30]. It is shown in Figure S10 as red triangles. We applied the model shown Figure 6, that is, CE and tCE where spectral diffusion is computed using the analytical expression of Eq. 3. In these conditions (lower field and possibly stronger saturating field), the contribution of the SE is more pronounced than at 14.1 T, so it was included in the simulation. The black lines show the individual simulated DNP profiles and their sum. The EPR line of the slow relaxing spins (dipolar-broadened and isolated) at thermal equilibrium and under saturation at a select frequency (grey and lines, respectively) is shown in the top right plot of each panel. The EPR line of the fast-relaxing spins (exchange-coupled pairs) is shown in the bottom right plot of each panel. The spectral diffusion length and relative contributions of the tCE, CE, and SE were manually fitted. The static magnetic field of 3.3476 and 6.9074 T were also let free to align the simulated and experimental profiles. The spectral diffusion length was fitted to 6 and 22 MHz at 3.3 and 6.9 T, respectively. For comparison, a spectral diffusion length of 22 MHz was obtained at 14.1 T (see Table S2).

The model is in good agreement with the experimental data at 6.9 T (see Figure S10b). At 3.3 T, the model reproduces most of the features (see Figure S10a). However, the central negative absorptive feature is not reproduced by the model (highlighted in yellow in Figure S10a). This very feature was attributed to tCE by Bussandri *et al*.[30] It is possible that the fast-relaxing spins taking part into the proposed tCE feature are spin species different from P1 centers, as suggested by Bussandri *et al*.[30]

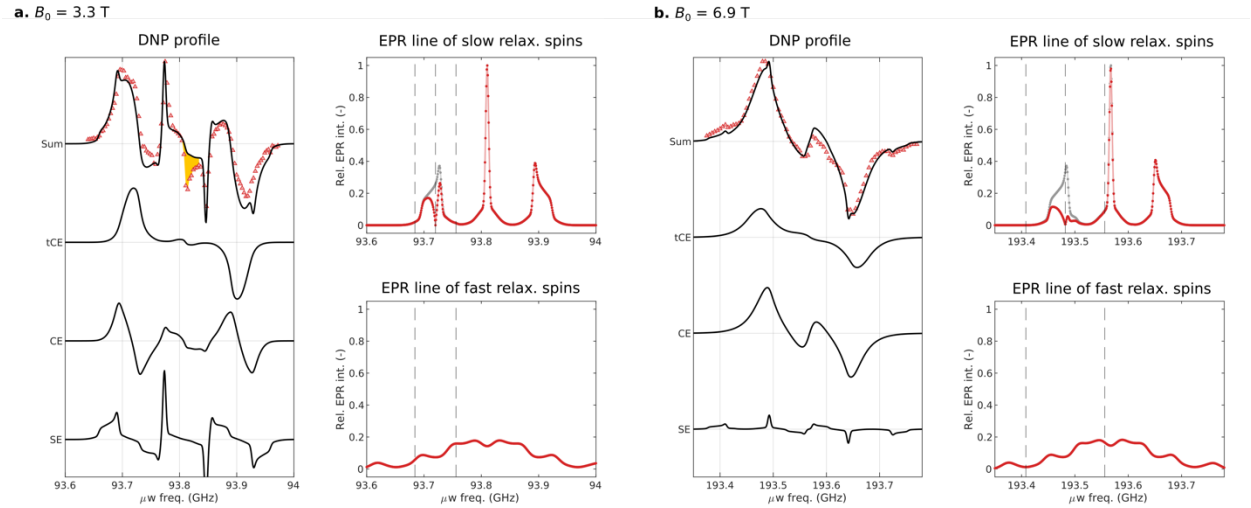

Figure S10: **a,b**. Comparison of the experimental DNP profiles reported in Ref. [30] at 3.3 and 6.9 T, respectively, and room temperature in static mode for the same diamond sample as in this study. The top plots on the right of each panel show the EPR line of the slow-relaxing spins at thermal equilibrium and under saturation at a select frequency, represented as grey and red lines, respectively. The black dashed lines represent the microwave irradiation frequency and the two corresponding positions for triple-spin flips partners. The bottom plots on the right of each panel show the EPR line of the fast-relaxing spins at thermal equilibrium. The black dashed lines represent the two positions for triple-spin that correspond to the irradiation frequency on the plot of the slow-relaxing spins. The yellow area in panel a highlights the region where the model does not reproduce the experimental data.

e. Transition distribution for exchange-coupled P1 pairs

The EPR spectrum of the exchange-coupled was simulated using EasySpin function *pepper*, with the option that separates the EPR spectrum into the components corresponding to different transitions (option *separate* set to the value *transitions*) for a magnetic field of 14.1 T and using the parameters given in the Methods section of the paper. The resulting spectra are shown in the left panel of Figure S11 (as colored lines). The sum of all the components corresponds to the whole EPR line and is shown as a black line. The transition intensities were calculated by integrating the individual components. Their relative contributions of the transitions are shown on the right panel of Figure S11 as blue dots, ordered in descending intensity. The cumulative distribution of the blue curve in Figure S11 is shown in black on the same plot. This plot shows that the most intense transition only contributes to about 5% of the total EPR line and the 20 first most intense transitions account for less than 50% of the total EPR line.

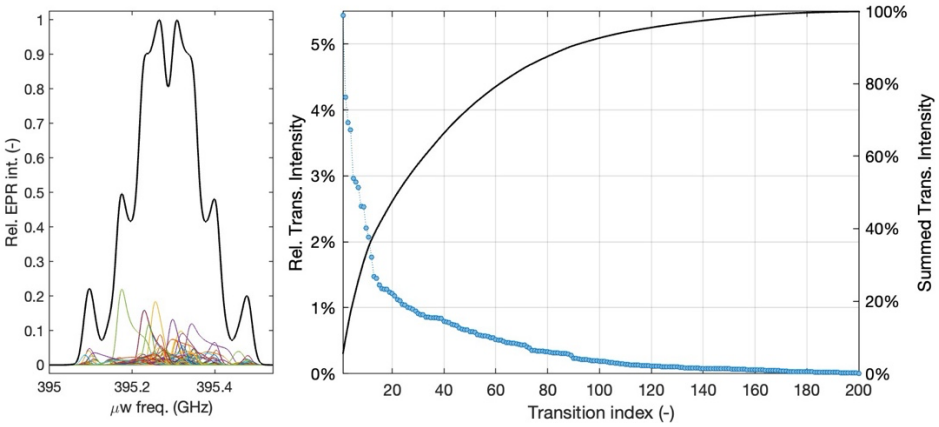

Figure S11: Decomposition into individual transitions of the powder-averaged EPR spectrum of exchange-coupled P1 spin pairs. Left: EPR spectrum of the individual transitions (colored lines) and sum of all transitions (black line). Right: Transition intensities (obtained by integrating the spectra on the left) ordered from most to least intense (blue dots) and cumulative distribution of the transition intensities (black line).